Experimental study of muon pairs produced by 252-GeV pions on tungsten

J. S. Conway,* C. E. Adolphsen,† J. P. Alexander,‡ K. J. Anderson, J. G. Heinrich, J. E. Pilcher, and A. Possoz
Enrico Fermi Institute and Department of Physics, The University of Chicago, Chicago, Illinois 60637

E. I. Rosenberg
Ames Laboratory and Department of Physics, Iowa State University, Ames, Iowa 50011

C. Biino,§ J. F. Greenhalgh,** W. C. Louis,†† K. T. McDonald, S. Palestini,§ F. C. Shoemaker, and A. J. S. Smith
Joseph Henry Laboratories, Department of Physics, Princeton University, Princeton, New Jersey 08544
(Received 8 July 1988)

We present the results of a study of muon pairs with invariant masses greater than 4.05 GeV/c^2 produced in high-energy pion-nucleon interactions. The production cross section together with the inferred pion and nucleon structure functions are reported and compared with other experiments and with QCD predictions. The transverse-momentum distributions are also presented. Finally, the full angular distribution in $\cos\theta$ and ϕ is given as a function of mass, Feynman x, and transverse momentum. Longitudinal photon polarization is seen in the lower portion of the mass range at high x_π. This result is compared with a higher-twist model.

I. INTRODUCTION

The production of massive lepton pairs in hadronic interactions is an important probe of the internal dynamics of hadrons. It is well established that one of the dominant production mechanisms is the Drell-Yan process[1] in which the pair is produced through the electromagnetic annihilation of a constituent quark and antiquark in the colliding hadrons. In the context of this model one can extract the momentum distributions (structure functions) of the quarks in the interacting hadrons.

This method tests the process independence of the nucleon structure functions measured in deeply inelastic lepton scattering and is one of the few means of determining the quark structure functions of unstable hadrons such as pions and kaons. Additionally, in lepton-pair production one may examine the angular distribution of the final-state particles to determine the polarization of the virtual photon. This measurement is analogous to the determination of σ_L/σ_T in deeply inelastic lepton scattering.

This paper presents the analysis of a large sample of muon pairs produced by a 252-GeV π^- beam interacting in a tungsten target. This is the bulk of the data collected by the E615 Collaboration at Fermilab. Data were also obtained with an 80-GeV π^- beam and with a 252-GeV π^+ beam. The results from the analysis of the 80-GeV sample have been presented elsewhere.[2] In this analysis we restrict attention to the 36 000 continuum muon pairs of invariant mass greater than 4.05 GeV/c^2. This data sample is especially rich in pairs produced at large x_F. Full details of the analysis may be found in Ref. 3.

In the rest of this section we introduce briefly the theoretical models of lepton-pair production, including kinematics, the Drell-Yan model, and QCD modifications. In Sec. II the experiment is briefly described, and in Sec. III the important features of the analysis are discussed. Sections IV–VI present the experimental results, divided into three main topics.

Section IV presents results for the pion and nucleon structure functions obtained from the dependence of the cross section on mass and longitudinal momentum. In Sec. V the dependence of the cross section on the pair transverse momentum is reported as a function of mass and x_F. Finally, the dimuon angular distribution is analyzed in the pair rest frame and its kinematic dependence determined. Good acceptance in these angular variables is one of the unique features of this experiment.

A. Kinematics

Figure 1 depicts the process $\pi^- N \to \mu^+ \mu^- X$ in the center-of-mass frame of the colliding hadrons. Here the virtual photon associated with the muon pair recoils against the unobserved final-state hadronic debris. We define $m_{\mu\mu}$ to be the invariant mass of the lepton pair, and p_L and p_T to be the components of the photon momentum parallel and perpendicular, respectively, to the incident pion momentum. The scattering is independent of the laboratory azimuthal angle of the pair $\phi_{\rm lab}$, since in this experiment the beam and target are unpolarized. The longitudinal-momentum fraction x_F (Feynman x) of the pair is defined as

$$x_F = 2p_L/\sqrt{s} \ .$$

This definition facilitates comparison with earlier experiments but the reader should note that the kinematic maximum of x_F is less than unity, depending on the pair mass and transverse momentum. In the rest of the paper we use the limit $x_F \to 1$ to refer to the upper kinematic limit.

 ©1989 The American Physical Society

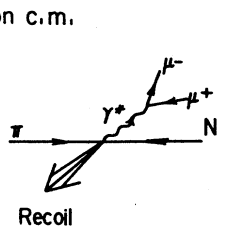

FIG. 1. Kinematics of muon-pair production in the hadron center-of-momentum frame.

The dimensionless quantities x_π and x_N are defined by the equations

$$x_F = x_\pi - x_N$$

and

$$x_\pi x_N = \tau = m_{\mu\mu}^2/s \ ,$$

where $s=(p_\pi+p_N)^2$ is the center-of-mass energy squared. (Here p_π and p_N are the hadron four momenta.) These equations together imply

$$x_{\pi,N} = [\pm x_F + (x_F^2+4\tau)^{1/2}]/2 \ .$$

The quantities x_π and x_N can be interpreted as the momentum fractions of the annihilating quarks in the hadrons, neglecting transverse momentum and quark mass, as s becomes very large.

The remaining degrees of freedom are those describing the orientation of the muons in the pair rest frame (see Fig. 2). The variables $\cos\theta$ and ϕ describe the direction of the μ^+ relative to a set of axes in this frame. Ideally, one would measure $\cos\theta$ and ϕ relative to the quark-antiquark annihilation axis, but this is impossible because the individual transverse momenta of the quarks are unknown. Several choices of axes are commonly used. In all these frames the y axis is taken to be perpendicular to the plane formed by the pion and nucleon directions. The different frames are then related by a rotation about this y axis. One set of axes is the t-channel, or Gottfried-Jackson frame, in which the z axis is taken to be the pion

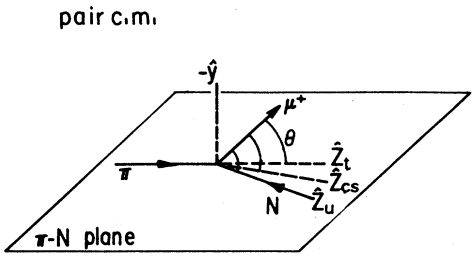

FIG. 2. Definition of angles in the muon-pair rest frame.

direction in the muon-pair rest frame. For the u-channel frame the z axis is chosen to be antiparallel to the nucleon direction, while in the Collins-Soper frame the z axis is the bisector of the angle between the t- and u-channel z axes. As $p_T \to 0$ the frames become identical and ϕ becomes undefined. The angle 2β between the z axes in the t- and the u-channel frames is, to very good approximation, given by $\beta=\arctan(p_T/m_{\mu\mu})$. In this experiment a typical value of β is ~ 0.2 rad.

B. Drell-Yan model

Drell and Yan[1] proposed that muon pairs with large invariant mass from hadron-hadron interactions are produced through the electromagnetic annihilation of constituent quarks and antiquarks. For massless spin-$\frac{1}{2}$ quarks, the annihilation cross section is given by

$$\sigma_{q\bar{q}} = \frac{4\pi\alpha^2}{3m_{\mu\mu}^2} e^2 \ ,$$

where e is the quark charge. If $q_\pi^i(x_\pi)$ $[\bar{q}_\pi^{\,i}(x_\pi)]$ is the probability density for finding a quark [antiquark] of flavor i, any color, and momentum fraction x_π in a pion, and if $q_N^i(x_N)$ is a similar function for the nucleon, then the Drell-Yan formula reads

$$\frac{d^2\sigma_{\rm DY}}{dx_\pi dx_N} = \frac{4\pi\alpha^2}{9m_{\mu\mu}^2} \sum_i e_i^2 [q_\pi^i(x_\pi)\bar{q}_N^{\,i}(x_N) + \bar{q}_\pi^{\,i}(x_\pi) q_N^i(x_N)] .$$

This relationship provides a means to measure these functions for the pion and nucleon. In this expression the transverse momentum of the pair has been integrated over. The Drell-Yan cross section also leads to the result that

$$\frac{m_{\mu\mu}^3 d^2\sigma}{dm_{\mu\mu}dx_F} = f(x_F,\tau) \ ,$$

with f a function of x_F and τ only, independent of s.

The angular distribution of the μ^+ in the pair rest frame can be written

$$\frac{d^2\sigma}{d\cos\theta\, d\phi} \propto 1+\lambda\cos^2\theta+\mu\sin 2\theta\cos\phi+\nu/2\sin^2\theta\cos 2\phi \ ,$$

where λ, μ, and ν are functions of the other kinematic variables. In the Drell-Yan model the assumption of massless quarks implies that the virtual photon is transversely polarized so that $\lambda=1$ and $\mu=\nu=0$, and one has

$$\frac{d^2\sigma}{d\cos\theta} \propto 1+\cos^2\theta \ .$$

This relation holds only when θ is measured relative to the true quark-antiquark annihilation axis. As indicated above, this axis is not directly measurable because of the unobserved individual transverse momenta of the quarks within the hadrons. The influence of this intrinsic transverse momentum on λ, μ, and ν has been evaluated and the expected effects are very small.[4]

A general relation based on the assumption of massless quarks arises for the angular distribution parameters. It is analogous to the Callan-Gross relation in deeply inelas-

tic scattering.[5] The relation

$$1-\lambda=2\nu$$

is expected to hold in any reference frame, and is unmodified by QCD corrections described below, but is influenced by intrinsic transverse momenta such that in the Collins-Soper frame[4]

$$1-\lambda=2\nu+\frac{8\langle k_{T\pi}^2\rangle\langle k_{TN}^2\rangle}{m_{\mu\mu}^2\langle p_T^2\rangle} .$$

C. QCD modifications

The Drell-Yan model successfully accounts for many features of muon-pair production including the π^+/π^- production ratios, the agreement between nucleon structure functions measured in deeply inelastic scattering and muon-pair production, the overall angular distributions, and the observed scaling behavior. The original model, however, ignored transverse momenta and failed to account for the observed size of the total cross section. These shortcomings motivated detailed considerations of the QCD corrections. Several first-order QCD processes are expected to modify the basic Drell-Yan picture. Their Feynman diagrams are illustrated in Fig. 3. All involve the emission or absorption of a free gluon and fall into two categories: annihilation with gluon emission ($q\bar{q}g$ diagrams) and quark-gluon scattering (qg diagrams).

The QCD modifications have been treated to several levels of approximation. First, certain classes of subprocesses contribute logarithmic corrections to the cross section. The largest logarithmic terms from each order of α_s can be summed explicitly and this constitutes the leading-log approximation (LLA) to the cross section. In this approximation it has been shown that the Drell-Yan cross section is modified by making the quark densities scale dependent. The cross section becomes[6]

$$\frac{d^2\sigma_{\rm LLA}}{dx_\pi dx_N}=\frac{4\pi\alpha^2}{9m_{\mu\mu}^2}\sum_i e_i^2[q_\pi^i(x_\pi,m_{\mu\mu}^2)\bar{q}_N^i(x_N,m_{\mu\mu}^2) + q\leftrightarrows\bar{q}]$$

and the scaling law in the leading-log approximation is

$$\frac{m_{\mu\mu}^3 d^2\sigma_{\rm QCD}}{dm_{\mu\mu}dx_F}=f(x_F,\tau,\ln(m_{\mu\mu}^2/\Lambda^2)) .$$

Thus, in the leading-log approximation the only change to the Drell-Yan cross section is the introduction of $m_{\mu\mu}^2$-dependent structure functions. For the nucleon these are the same Q^2-dependent structure functions measured in deeply inelastic scattering.

The next-to-leading-log (NLLA) corrections include, in addition, all first-order α_s terms arising from the processes of Fig. 3. This leads to an overall cross section approximately 1.7 times larger than the LLA (Ref. 6). The large correction arises primarily because the deeply inelastic structure functions are measured with spacelike photons while the Drell-Yan process involves timelike photons. This increase, referred to as the K factor, is approximately

$$K\simeq 1+\frac{\alpha_s}{2\pi}\frac{4}{3}\pi^2 ,$$

and is roughly independent of $m_{\mu\mu}^2$ and x_F, except near the kinematic limits $\tau\to 1$ and $x_F\to 1$ (Ref. 6).

First-order QCD corrections also affect the angular distributions. Several authors[4,7] have calculated the angular distribution coefficients for these diagrams. The relation $1-\lambda=2\nu$ (massless quarks) is assumed to hold implicitly in all these calculations. Qualitatively, the coefficients μ and ν are expected to increase proportionally to $p_T/m_{\mu\mu}$ and $(p_T/m_{\mu\mu})^2$, respectively.[5] Thews[7] calculated the coefficients averaging over the longitudinal momenta of the pair, for the cases of annihilation with gluon emission, and quark-gluon scattering. He reports for λ in the t-channel frame

$$\lambda_{q\bar{q}g}=\frac{1-\rho^2+\rho^4}{1+3\rho^2+\rho^4},\quad \rho\equiv\frac{p_T}{m_{\mu\mu}} ,$$

and

$$\lambda_{qg}=\frac{1-3\rho^2+5\rho^4}{1+9\rho^2+5\rho^4}$$

for the two subprocesses. These formulas are independent of the quark distributions only when integrated over a symmetric region in x_F at a given $m_{\mu\mu}$. The particular dependence of λ on x_π and x_N relies on knowledge of the quark and gluon distribution functions. For μ the results of Thews for the QCD subprocesses are

$$\mu_{q\bar{q}g}=\frac{\rho(1-\rho^2)}{2(1+\rho^2)^2}$$

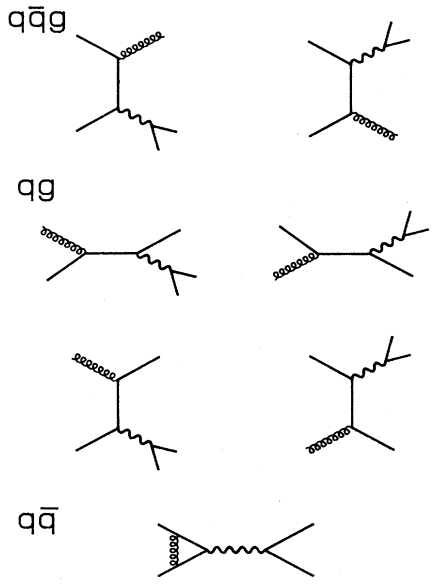

FIG. 3. First-order QCD processes contributing to muon-pair production.

and

$$\mu_{qg}=\frac{\rho(1-\rho^2)\{\rho^2+[\rho+(1+\rho^2)]^2\}}{2(1+\rho^2)^2(1+5\rho^2)} .$$

D. Higher-twist effects

Another QCD prediction involves the production of muon pairs near the limit $x_F\to 1$. Berger and Brodsky argue that from kinematics alone, as this limit is approached, the annihilating quark or antiquark in the pion goes off shell and a component of longitudinal photon polarization arises.[8] Their QCD model estimates the magnitude of the effect. They represent the process by a single-gluon exchange in the pion between the annihilating valence antiquark and the "spectator" valence quark. The process is shown in Fig. 4. They conclude that the pion structure function contains a scaling term associated with an angular dependence of $1+\cos^2\theta$ and a nonscaling term with a $\sin^2\theta$ variation. Specifically, they calculate that as $x_F\to 1$, in the t-channel frame

$$d\sigma \propto (1-x_\pi)^2(1+\cos^2\theta)+\frac{4x_\pi^2\langle k_T^2\rangle}{9m_{\mu\mu}^2}\sin^2\theta$$
$$+\frac{2}{3}\left\langle\frac{k_T^2}{m_{\mu\mu}^2}\right\rangle^{1/2} x_\pi(1-x_\pi)\sin 2\theta\cos\phi ,$$

where here the scale parameter $\langle k_T^2\rangle$ characterizes the mean-square transverse momentum of the annihilating antiquark.[8] Integrating over the azimuthal angle ϕ, one is left with only the first two angular terms. Integrating over $\cos\theta$ implies that the quark density function of the pion, $q_\pi(x_\pi)$, is

$$q_\pi(x_\pi)\underset{x_F\to 1}{\to}(1-x_\pi)^2+\frac{2x_\pi^2\langle k_T^2\rangle}{9m_{\mu\mu}^2} .$$

This shows explicitly the presence of a term in the structure function varying like $1/m_{\mu\mu}^2$ and having a nonzero intercept at $x_\pi=1$.

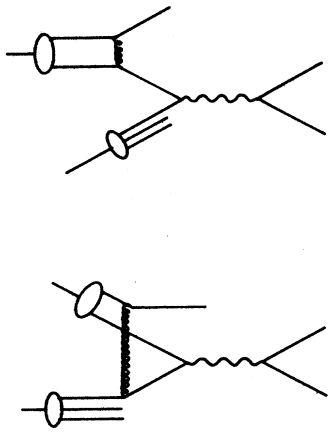

FIG. 4. Diagrams calculated by Berger and Brodsky in their higher-twist model.

II. EXPERIMENTAL APPARATUS

This experiment, designated E615, was carried out in the Proton-West High Intensity Area at Fermilab. The apparatus has been described in detail elsewhere.[9] Figure 5 shows the general layout of the apparatus. The secondary hadron beam was produced with primary protons from the superconducting accelerator. It impinged on the experimental target located just upstream from a large-aperture dipole magnet. This dipole or "selection" magnet was filled with low-Z material to absorb the beam and secondary hadrons. In addition it swept low-energy muons out of the active region of the detector. The muon spectrometer itself was a system of proportional chambers and drift chambers, together with a second large dipole magnet. A multilevel electronic trigger used information from scintillator hodoscope arrays to identify high-mass pairs in the detector.

A. Beam and beam monitors

The secondary hadron beam was produced at an angle of 0° by 800-GeV protons striking a Be target. For the bulk of the data collection, the accelerator operated with a 33% duty cycle, producing a 20-sec spill every minute. The composition of the beam was not measured or tagged directly because the beam intensity of 2×10^8/sec was too high for such a measurement. The hadronic composition at the experimental target is estimated from the measurements of Atherton *et al.*[10] as 92.8% π^-, 5.5% K^-, and 1.7% $\bar{p}$.

The halo-muon component was reduced with spoiler magnets and shielding. These muons comprised about 2% of the total number of beam particles. Accidental coincidence of a halo muon with a muon of opposite sign from the experimental target, could mimic real prompt dimuon events. Since this was the largest source of background in the experiment, a significant effort was made to reduce this component of the beam using the spoiler magnets and halo-tagging scintillators.

The integrated beam flux was measured with three separate ionization chambers. Two of these were segmented into five annuli with individual readouts. The chambers were calibrated in special runs during which thin copper plates were placed in the beam downstream from the chambers. The production of ^{24}Na was measured and from the known cross section the total number of hadrons per ion chamber count was calculated to within about ±15%. The live time of the experiment was monitored by two devices. The first was an atmospheric-pressure Cherenkov counter situated in the beamline. The second was a three-counter telescope oriented at 90° to the beam, pointing at the center of the target. This device gave one count for every 10^4 pions and was thus less sensitive to beam time structure but more sensitive to beam position.

The beam momentum was measured during special low intensity runs with a system of twelve drift-chamber planes and a carefully measured beamline dipole magnet. The resulting momentum used in the analysis was 252 GeV/c, with a systematic uncertainty of 2 GeV/c. The beam was also measured to have a divergence of about

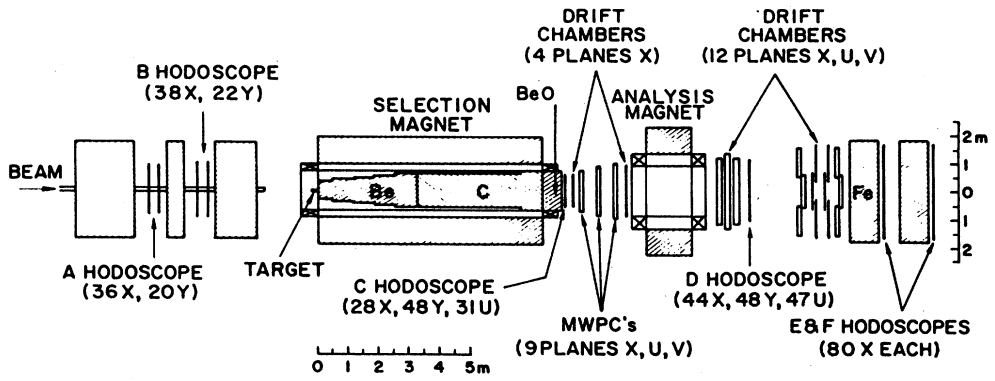

FIG. 5. Layout of the E615 apparatus.

0.3 mrad, a momentum spread of 25 GeV/c full width at half maximum (FWHM), and an effective angle of 0.7 mrad in the horizontal plane,with respect to the nominal direction in the laboratory-based coordinate system used for the analysis.

B. Shield, target, absorber, and selection magnet

Figure 6 shows the upstream section of the experiment, including the target, absorber, and selection magnet. A concrete and steel veto shield was located upstream of the target to absorb low-energy hadrons and electrons produced by upstream beam losses.

The target was a 20-cm-long, 5-cm-diameter cylinder of tungsten alloy. This corresponds to about 1.7 pion elastic interaction lengths, so that more than 80% of the pions interacted in the target. It was located 46 cm upstream of the shielding material.

The first section of hadron shield consisted of a 47-cm-thick stack of sintered beryllium-oxide bricks placed against the upstream edge of the selection-magnet pole face. As shown in Figs. 5 and 6, the magnet was filled with beryllium in the upstream section and graphite in the downstream part. The final element of the absorber was another stack of beryllium-oxide bricks. The absorber was entirely uniform in the plane transverse to the beam, with no central plug of high-Z material as used in some previous experiments. This facilitated the detection of muons produced at a small angle with respect to the beam.

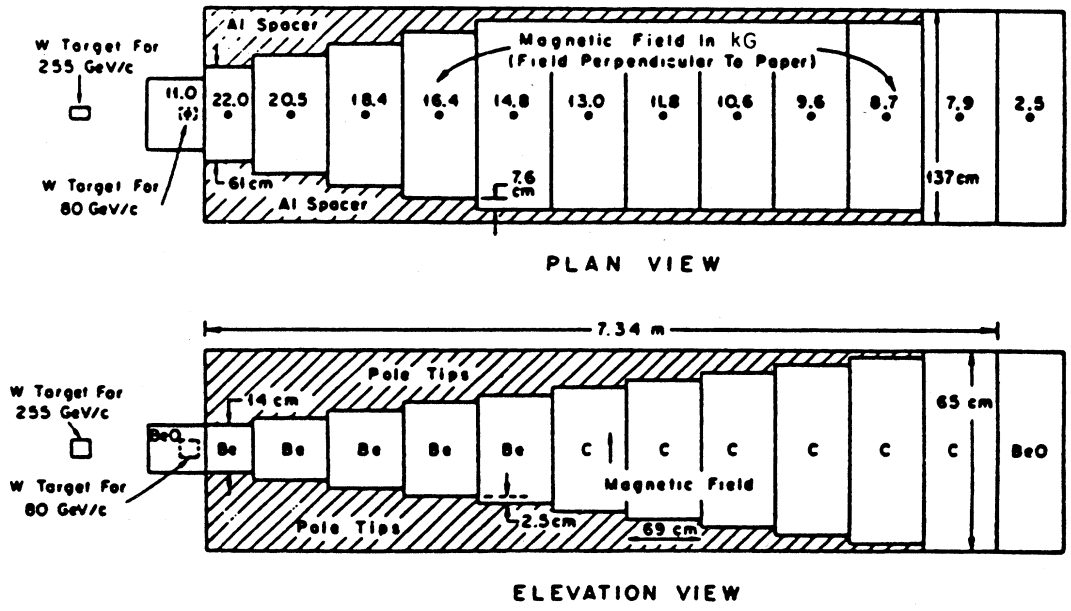

FIG. 6. Schematic diagram of upstream portion of apparatus.

The absorber strongly attenuated the hadronic and electromagnetic debris produced in the target and the upstream portion of the shield. Material of low atomic number was used to minimize multiple Coulomb scattering and energy loss of the detected muons. The target was placed away from the absorber to facilitate identification of events produced in the target, as opposed to the absorber. After analysis cuts, no more than 1% of the events originate in the shield.

The field of the selection magnet swept low-energy muons and low-mass muon pairs out of the active region of the spectrometer. Muons from high-mass pairs were focused towards the spectrometer, enhancing their acceptance. To best achieve this goal the gap between pole faces was tapered, being smaller at the upstream end. This concentrated the field integral near the target and provided the greatest possible lever arm for displacing the particle trajectories in the analyzing spectrometer. Figure 6 shows these design details. The transverse-momentum kick of the magnet was 3.14 GeV/c in the horizontal plane. The magnet aperture was 0.61 m wide by 0.14 m high at the upstream face and 1.37 m wide by 0.65 m high at the downstream end.

The field of the magnet was measured in most of its volume using the Fermilab ziptrack, a device in which three mutually perpendicular flux coils were fixed to a cart which moved inside an aluminum beam under computer control.

C. Spectrometer

The momentum analyzing spectrometer consisted of a system of wire chambers upstream and downstream of a second dipole magnet, as depicted in Fig. 7. Proportional chambers and drift chambers were used to provide a total of 25 points per track. The chamber wires were oriented either vertically (perpendicular to the bend plane) or at a small angle ($<20°$) to the vertical. The analyzing magnet for the spectrometer was a large air-gap (0.92 m$\times$1.82 m$\times$1.6 m) dipole with an 860-MeV/c transverse-momentum kick. Its field was also measured with the Fermilab ziptrack and an absolute calibration made with an NMR probe.

D. Trigger

During data collection the trigger electronics initiated event readout using the pattern of struck scintillators in the hodoscope banks. The design of these hodoscopes is shown in Fig. 8. The logic for the trigger was hierarchi-

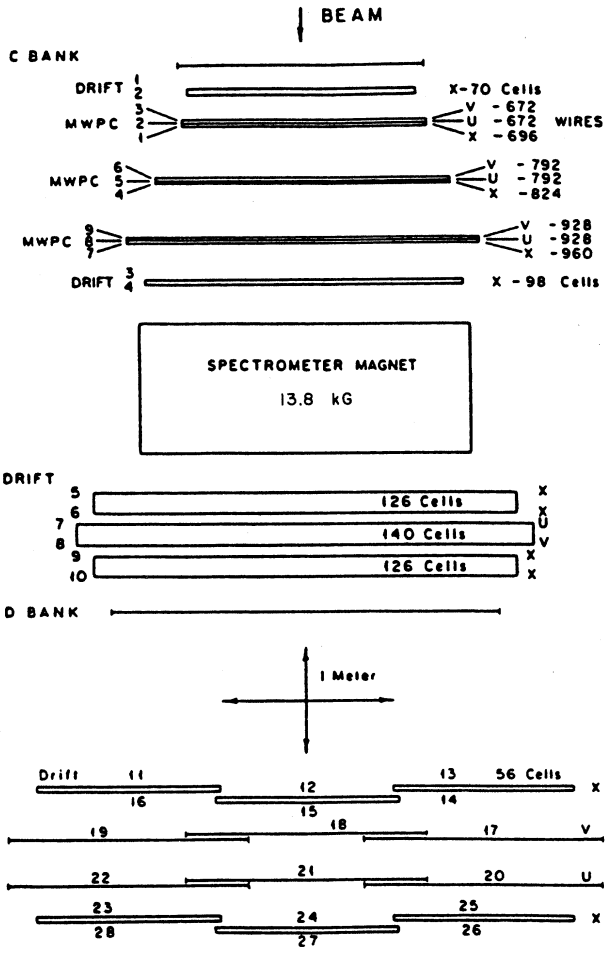

FIG. 7. Schematic diagram of spectrometer portion of apparatus.

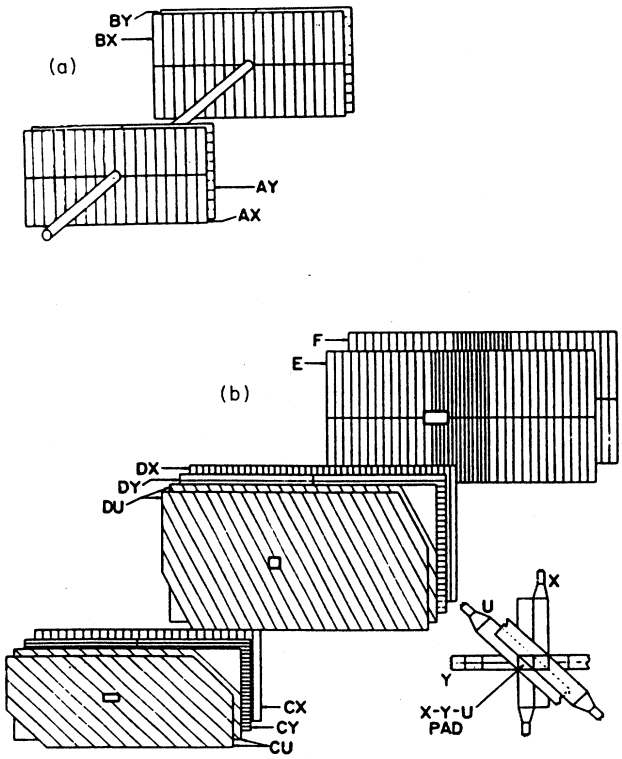

FIG. 8. Design of hodoscope planes showing: (a) veto planes; (b) trigger planes.

cal, organized in three levels of increasing complexity. Events with muons outside the beam pipe were vetoed by the A and B hodoscope banks. Level 1 of the trigger required at least two muons in the detector. Level 2 required two muons which projected back to the target in the nonbend (vertical) plane. Level 3 compared the pattern of struck counters with acceptable patterns, stored in a memory lookup table, for high-mass pairs. The tables of acceptable pair combinations were arrived at through a combination of Monte Carlo calculation and, once actual data were available, off-line analysis.

The efficiencies of all the hodoscope counters were measured using level-1 triggers; every thousandth of which was recorded as a prescaled trigger along with the normal level-3 events. Tracks were used for the efficiency determination if their associated counters were not necessary to the trigger, and if they satisfied stringent quality requirements. These quality requirements approximated those of the dimuon sample. The efficiencies as a function of position were then determined from these data. The typical overall plane efficiences were 99%. The inefficiencies tended to be near the ends of the counters, which made the CY and DY scintillator efficiencies (Fig. 8) more critical since the ends of these counters were in the center of the detector.

III. EVENT ANALYSIS

This section describes the method used to extract the differential cross sections. The process can be divided into four parts: event reconstruction, detector acceptance correction (Monte Carlo simulation), background determination, and overall normalization.

A. Event reconstruction

The data reduction proceeded in several stages. First, events were subjected to a simple off-line selection which added requirements in the E and F scintillation-counter planes to the on-line requirements of the level-3 trigger. An estimate of the pair mass was made using the scintillator information and events were rejected if they contained no pair with mass greater than 2.0 GeV/c^2. Next, tracks were reconstructed in the wire chambers and an upstream vertex position calculated. These steps are described in more detail below.

1. Track finding

The track-finding algorithm took the raw wire-hit information for each event and determined the trajectories of all the particles passing though the spectrometer.

The first step was to find the straight-line track segment in the upstream part of the spectrometer. Struck scintillators in the C and D planes were used to define a "road" through the region and the nine proportional chamber planes were searched for a track. The noise rates in these detectors were the lowest and the efficiency the highest. The resulting track segment was then projected into the upstream drift chambers to find the associated hits there and hence to improve the resolution. Finally, the segment was projected to an intercept at the midplane of the spectrometer magnet. This point together with the downstream hodoscope hits was used to determine the road for the downstream track search.

The only subtle feature of the track finding was to accommodate extra hits close to the actual track. These could arise from delta rays. The track finder chose those hits within the road which minimized the χ^2 for a straight-line fit. The candidate track was required to contain as many points as possible, consistent with an acceptable χ^2 confidence level.

The upstream and downstream track segments were combined into a global fit which required the segments to meet near the midplane of the spectrometer magnet. Because of the high level of redundancy in the measured points (25 per track) and good chamber efficiency, the track-finding efficiency was 99.7%.

The spatial resolution achieved in the proportional chambers was on average 600 μm. That of the drift chambers was 250 μm. This led to a momentum resolution of $\sigma_p/p = 0.01\% \times p$, with p in GeV/c.

2. Vertex fit

The vector momenta of two oppositely charged muons downstream of the selection magnet were used to select pairs originating in the target, and to determine the vector momenta of the tracks at the production point. A constrained fit to the mean production point in the target was performed, and pairs with a χ^2 confidence level of less than 2% in either the x-z or y-z projections were eliminated. Allowance was made for multiple scattering and energy loss in the hadron absorber, and for deflection by the nonuniform magnetic field of the selection magnet. Since the general problem was too difficult to solve analytically for each event, a Monte Carlo calculation was performed to simulate the muon transport through the selection magnet and hence to calculate coefficients in a parametrized form for the initial positions, slopes, and track momenta. The simulation was based on the measurements of the magnetic fields and the exact absorber geometry. The results were checked with actual data by examining the transverse displacements of reconstructed tracks at the target plane as a function of momentum and angle. No systematic shifts were observed.

A second test was the comparison of the reconstructed masses for the J/ψ and Υ resonances with the known values. The agreement for the J/ψ was good to 0.8% in absolute mass or 14% of the rms mass resolution itself. This is consistent with expected uncertainty in the absolute field integrals. The mass comparison at the Υ showed no evidence of a shift with a sensitivity of $\sim 1\%$. Reference 3 shows these comparison in detail.

3. Final selection criteria

Several requirements were placed on reconstructed data to remove ambiguities and to reduce backgrounds. First it was required that an event contain one and only one prompt pair reconstructed to the target. A prompt pair was defined as two oppositely charged muons with individual track momenta less than 260 GeV/c and a

combined momentum less than 280 GeV/c. The loss of good events was 7.4% and this was corrected at a later stage.

For events satisfying this first criterion, each track was required to be within the fiducial volume of the detector; that is, each track was required to not hit the steel in the magnets or pass through the holes in the counter banks shown in Fig. 8. The hodoscope counters associated with both tracks were required to satisfy all three on-line trigger requirements as well as the preliminary off-line selection described above. By "associated" it is meant that the reconstructed track was projected onto each counter bank and the counter at this position was checked to see if it had a hit. If not, and the projected position was within a few millimeters of a neighboring counter which had a hit, this counter was used instead, thus taking into account multiple scattering and position resolution.

B. Background determination

The background level in most kinematic distributions is no more than a few percent. Only at intermediate p_T or $|\cos\theta| > 0.9$ does the background become significant and a simple cut on $|\cos\theta|$ eliminates most of it. Its main source is the accidental pairing of single muons associated with different beam particles. Typically, the background events were the result of a beam-sign muon of large momentum in accidental coincidence with a lower momentum muon from an interaction in the target.

To estimate the background characteristics, single tracks from the prescaled level-1 triggers were randomly paired. These simulated pairs showed the expected clustering near $|\cos\theta| = 1$ and $\phi_{\rm lab} = 0$ as seen in the actual event distributions. The normalization of this simulated background was chosen to produce agreement between the observed event yield and that of the simulated data plus background, for events with either muon at an angle of less than 8 mrad to the beam. The background is strongest in this region.

Figure 9 shows for different kinematic variables the ratio of background-corrected data to accepted Monte Carlo events. Also shown is the size of the background subtraction. The flatness of the background corrected plots, particularly the $\phi_{\rm lab}$ ratio, shows that the background subtraction works quite well and that the background is very well understood. One is even less sensitive to the background with a cut on $|\cos\theta|$. As described below, such a cut was imposed with the value depending slightly on the physics issue under study.

C. Acceptance calculation

A Monte Carlo simulation of the detector response was used to determine the acceptance. The initial muon trajectories were generated from an estimated differential cross section for the pair production and from the momenta of the beam pion and target nucleon. The latter arises from Fermi motion.[11] The production of dimuons from secondary and tertiary pions was included in the simulation, and the effect removed from the data as part of the acceptance calculation. The transport of the particles through the selection magnet and absorber was simulated in small steps along the beam direction. In the spectrometer region, hits in the hodoscope counters were simulated using the measured position-dependent efficiencies of the counters. Hits in the chambers were not simulated, but the chamber resolution was included by smearing the known trajectories of the muons. The simulated events were treated identically to the real events from this point on, including the vertex fit, trigger requirement, fiducial cut, etc. A record of the success or failure was kept for each event.

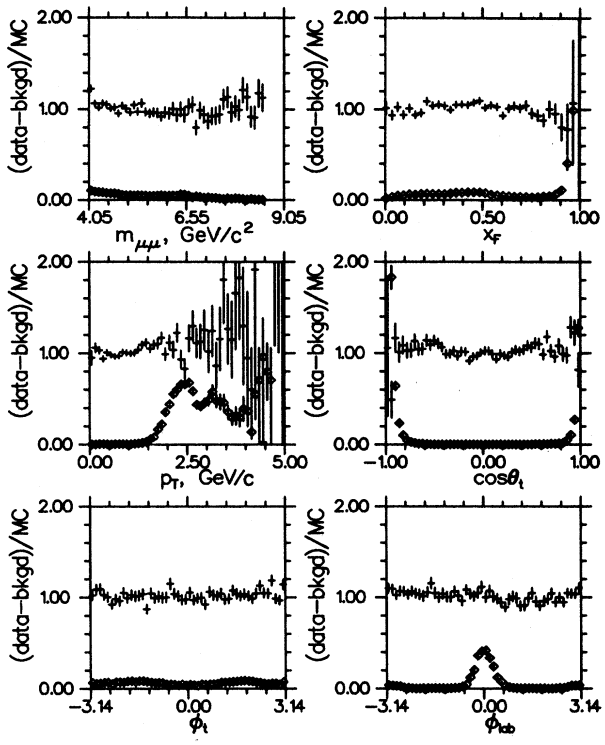

FIG. 9. Ratio of background-corrected data to accepted Monte Carlo events for the six final-state variables. Diamonds indicate the background level subtracted. The number of Monte Carlo events is approximately four times the data although the ratio has been rescaled to 1 for clarity.

Figure 10 shows the acceptance in each kinematic variable. The good acceptance at large x_F and at large $|\cos\theta|$ reflects the detector being active close to the beam. The acceptance calculation was checked by comparing real with simulated illuminations of various detector planes, and by comparing real with simulated kinematic distributions as shown in Fig. 9.

The corrected number of events n_c in any kinematic interval is defined as

$$n_c = \frac{n_t - n_b}{n_a} n_g \ ,$$

where n_t is the total number of observed events, n_b is the normalized number of background events, n_g is the number of generated Monte Carlo events, and n_a is the num-

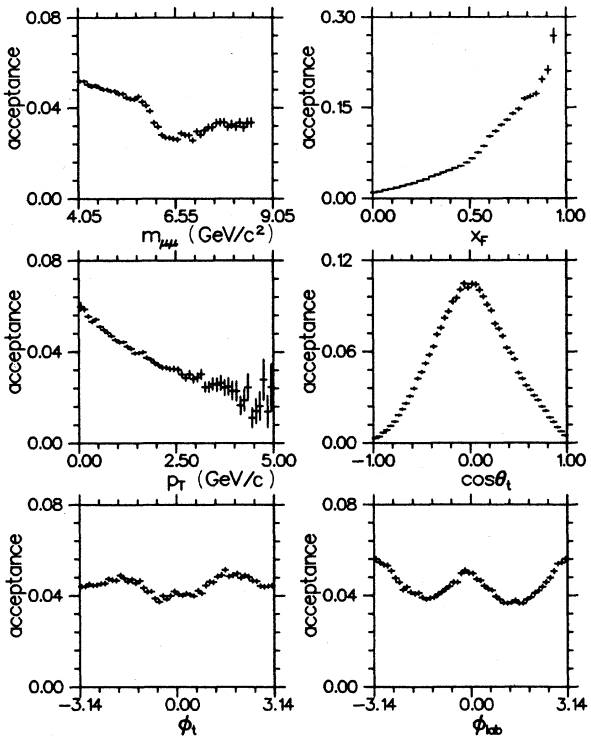

FIG. 10. Integrated detector acceptance for each kinematic variable.

ber of accepted Monte Carlo events. The errors in the number of observed and background events are taken to be those from a Poisson-distributed variable. This method correctly accounts for the experimental resolution of the reconstructed quantities only if the observed, background, and accepted Monte Carlo events are all subject to exactly the same cuts and the generated distributions are close to the true physical distributions. The generated distributions must also be close to the true physical ones for proper integration over kinematic variables not displayed.

The differential production cross section used in the Monte Carlo program was arrived at by an iterative procedure starting with the Drell-Yan model and earlier measurements of the pion and nucleon structure functions. Our data were used to modify the model. The final form (see Appendix A) includes the observed correlation of the angular distribution with x_π, p_T, and mass and the dependence of p_T on x_π and mass. For the results reported below, a systematic error of 5% is assigned to the acceptance computed in any interval. This is added in quadrature with statistical errors.

D. Normalization

Given the corrected number of events in a bin, the corresponding cross section also depends on the integrated luminosity. This was determined by two methods. From the integrated charge in the beam-line ion chambers, corrected for detector live time and beam attenuation in the target, we measure a luminosity of 4.01±0.8 events/(fb/nucleon) assuming a linear dependence of cross section on atomic weight of the target nucleus.

The integrated luminosity has also been determined from the number of J/ψ events detected, together with the known production cross section.[12] From J/ψ events contained in the prescaled level-1 sample, we calculate a luminosity of 3.99±0.6 events/(fb/nucleon), in very good agreement with the first method. Similar results are obtained from the J/ψ events in the level-3 sample. In the results which follow, a luminosity of 3.99±0.6 events/(fb/nucleon) is used.

IV. HADRONIC STRUCTURE FUNCTIONS

A. Mathematical formalism

1. Cross-section formula

The expression for the Drell-Yan cross section was given in Sec. I. Considering only u, d, and s quarks, including valence and sea quarks and all possible valence-valence, valence-sea, and sea-sea interactions, the expression becomes

$$\frac{d^2\sigma}{dx_\pi dx_N}=\frac{4\pi\alpha^2}{9s}\left[\frac{F_\pi^v(x_\pi)G_N(x_N)+F_\pi^s(x_\pi)H_N(x_N)}{(x_\pi x_n)^2}\right],$$

where $x_\pi x_N=m_{\mu\mu}^2/s$ and

$$F_\pi^v(x_\pi)=x_\pi\bar{u}^{\,v}(x_\pi)=x_\pi d^v(x_\pi),$$

$$F_\pi^s(x_\pi)=x_\pi\bar{u}^{\,s}(x_\pi)=x_\pi u^s(x_\pi)=\cdots=x_\pi\bar{s}^{\,s}(x_\pi),$$

$$G_N(x_N)=\frac{x_N}{9}\left[4\frac{Z}{A}u_p^v(x_N)+4\left[1-\frac{Z}{A}\right]d_p^v(x_N)+5u_p^s(x_N)\right],$$

$$H_N(x_N)=\frac{x_N}{9}\left[\left[1+3\frac{Z}{A}\right]u_p^v(x_N)+\left[4-3\frac{Z}{A}\right]d_p^v(x_N)+11u_p^s(x_N)\right].$$

Here $u_\pi^v(x_\pi)$ is the pion valence u-quark number density, $u_p^s(x_N)$ is the proton sea u-quark density, and so on. The quark densities are expressed in terms of those of the proton via the factors involving the atomic number Z and the atomic weight A of the target nucleus. We have taken $2s_p^s=u_p^s=d_p^s$, as supported by deeply inelastic scattering experiments.[13] The structure functions satisfy sum rules based on the number of valence quarks in the hadrons and the momentum fractions carried by the gluons. These are given in Appendix B.

2. Parametrization

We parametrize the structure function as

$$F_\pi^v(x_\pi)=A_\pi^v\left[x_\pi^\alpha(1-x_\pi)^\beta+\gamma\frac{2x_\pi^2}{9m_{\mu\mu}^2}\right],$$

$$F_\pi^s(x_\pi)=A_\pi^s(1-x_\pi)^\delta,$$

$$x_N u_p^v(x_N)=A_p^u x_N^\mu(1-x_N)^\nu,$$

$$x_N d_p^v(x_N)=A_p^d x_N^\mu(1-x_N)^{\nu+1},$$

$$x_N u_p^s(x_N)=A_p^s(1-x_N)^\zeta.$$

The sum rules constrain the normalization coefficients A_π^v, A_π^s, etc., as shown in Appendix B. The structure function form $x^\alpha(1-x)^\beta$ was motivated by Buras and Gaemers,[14] and was used in previous work. The term in the pion structure function proportional to $1/m_{\mu\mu}^2$ is motivated by the higher-twist prediction of Berger and Brodsky[8] discussed in Sec. I. In the proton structure function, the assignment of one higher power of $1-x_N$ for d_p^v over u_p^v is supported by data from deeply inelastic scattering experiments.[15]

3. $m_{\mu\mu}^2$ evolution

As described in Sec. I, the Drell-Yan cross-section expression can be retained in the presence of leading-log QCD corrections by allowing the quark density functions to be dependent on both x and $m_{\mu\mu}^2$. This is achieved in the Buras-Gaemers method[14] by making the parametrization exponents α, β, etc., functions of $m_{\mu\mu}^2$. The dependence is expected to be weak, with

$$\alpha=\alpha(\bar{s}),\quad \bar{s}=\ln\left[\frac{\ln(m_{\mu\mu}^2/\Lambda^2)}{\ln(m_{\mu\mu0}^2/\Lambda^2)}\right].$$

Following the prescription of Buras and Gaemers,[14] if the nth moment of the quark density distribution is given by

$$\langle q(x)\rangle_n=\int_0^1 dx\, x^{n-1}q(x),$$

then the evolution of the moments in QCD is given by

$$\langle q(x,m_{\mu\mu}^2)\rangle_n=\langle q(x,m_{\mu\mu0}^2)\rangle_n\exp(-\bar{s}\gamma_n),$$

where

$$\gamma_n=\frac{4}{33-2n_f}\left[1-\frac{2}{n(n+1)}+4\sum_{j=2}^{n}\frac{1}{j}\right]$$

for n_f quark flavors, with $\bar{s}$ defined above. From this relation one can derive equations of constraint on any desired number of parameters describing the evolution of the quark density exponents α, β, and so on as a function of $m_{\mu\mu}^2$, for a given Λ and $m_{\mu\mu0}^2$. For example, letting $\alpha(m_{\mu\mu}^2)=\alpha_0+\alpha_1\bar{s}$ and $\beta(m_{\mu\mu}^2)=\beta_0+\beta_1\bar{s}$ one can derive an expression for α_1 in terms of α_0, β_0, and s. It is important to note that in this procedure no new free parameters are introduced into the description of the pion structure function. Over the mass range of this experiment α and β are expected to vary by about 6% and 19%, respectively.

4. K factor

Previous experiments have showed that the basic Drell-Yan cross-section formula fails to explain the magnitude of the observed cross section by a factor of 2–3 (Refs. 16 and 17). This excess is termed the K factor, defined as the ratio of the observed differential cross section to a specific theoretical one:

$$K=\frac{d^2\sigma^{\rm obs}/dx_\pi dx_N}{d^2\sigma^{\rm th}/dx_\pi dx_N}.$$

Clearly K may be a function depending on x_π and x_N, or equivalently x_F and $m_{\mu\mu}$.

5. Structure-function determination

To extract the structure functions, the parametrized forms described above are fit to the data as a function of x_π and x_N. To display the results for the pion and nucleon separately and to compare the data with the fit and with other determinations, the data are projected on either the x_π or x_N axis by integrating over the second variable. The algebraic details are provided in Appendix C. The projected data points average over any evolution of the structure function with $m_{\mu\mu}^2$ within the kinematic region considered. As is suggested by the projection method, the structure function determination is quite insensitive to the details of the parametrization.

B. Analysis

To determine the structure functions, the x_π-x_N plane was divided into square cells and the event population in each cell obtained by correcting the observed number of events by the simulated background and the calculated acceptance. The results in this section were obtained with the requirement $|\cos\theta|<0.85$. The lost events were compensated by the acceptance calculation. All events were required to lie in the range $4.05<m_{\mu\mu}<8.55$ GeV/c^2 and $0.0<x_F<1.0$. Figure 11 shows the distribution of raw events, together with the grid of bins in x_π-x_N space and the region fit. The cell size is 0.02 by 0.02. For the sample of 252-GeV π^- data analyzed here, these cuts retain 27 977 $\mu^+\mu^-$ events, and involve a background subtraction of 110 events.

Some bins on the edges of the region are traversed by the $m_{\mu\mu}$ and x_F boundaries. In cases where the bin center is within the accepted region, the contents were rescaled to correspond to a fully enclosed bin using a factor determined with the Monte Carlo program; otherwise, the bin was excluded. We required that all bins used in the fit have an acceptance of at least 1%. The structure function parameters were obtained from a maximum-likelihood estimate for the bin contents.

The shape of the pion valence function F_π and the nucleon function G_N, defined above, can be extracted from the data with little ambiguity, particularly in the region above $x_\pi\sim0.3$ where the pion sea makes little contribu-

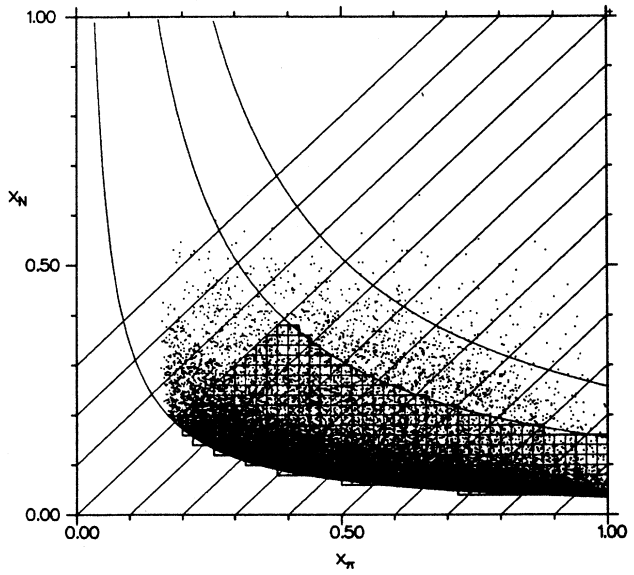

FIG. 11. Distribution of the 36000 events with $m_{\mu\mu} > 4.05$ GeV/c^2 in the x_π-x_N plane. The grid shows cells used in structure-function analysis and heavy lines delimit the region fit. Diagonal lines correspond to constant $x_F \equiv x_\pi - x_N$, and hyperbolas are curves of constant mass at values of 4.05, 8.55, and 11.05 GeV/c^2.

tion. They can be obtained almost directly using the projection method. Nevertheless, the shape of F_π at lower x_π and the overall cross-section normalization (K factor) are of some interest. These results are subject to a number of special considerations. The K factor, which is one of the parameters determined, is obviously affected by the 15% uncertainty in the integrated luminosity. More importantly, it is correlated with the parameters α, δ, and g_π which describe, respectively, the low-x_π region of the pion valence structure function, the pion sea, and the pion's gluon momentum fraction. The correlation follows from the normalization requirements for the quark number and momentum densities, as described above.

An independent determination of these parameters requires data at low x_π. For example, the region $x_\pi = 0.2$ to $x_\pi = 1.0$ covered in this experiment includes only about 30% of the valence-quark number-density integral and no other published data extend to appreciably lower x_π. Despite this limitation one can search for changes in normalization over the $\sqrt{\tau}$ region covered by this experiment, although the individual components in the normalization cannot be isolated.

The values of δ, the pion sea exponent, and g_π, the gluon momentum fraction are held fixed at values reported by Badier *et al.*[18] (NA3). They performed a simultaneous fit to π^+, π^-, and p data taken at 200 GeV and over the region $x_\pi > 0.15$. Their values are $\delta = 8.4 \pm 2.5$ and $g_\pi = 0.47 \pm 0.15$.

Similarly the values of g_p and ζ, the proton gluon-fraction and sea exponent, are best determined by other experiments. The values used here are held fixed at $g_p = 0.48$ and $\zeta = 9.0$, according to the parametrization of Purohit[19] [Chicago-Columbia-Fermilab-Rochester-Rockefeller (CCFRR) Collaboration] given in Appendix D.

This experiment is very well suited to measuring the shape of the structure function at high x_π as characterized by the parameters β and γ. At high x_π (high x_F), a good knowledge of the beam momentum is required. The residual uncertainty in the beam momentum of 1% is reflected in our assignment of systematic uncertainties to β and γ of ± 0.07 and ± 0.2. We have considered the influence of the treatment of Fermi momentum on these results. Since the nucleon structure function is large and slowly varying in the region of interest, Fermi motion has little effect.

C. Results

1. *Nucleon structure*

Figure 12 shows the results for the pion and nucleon structure functions determined in the region $x_F > 0$, $4.05 < m_{\mu\mu} < 8.55$ GeV/c^2, and $x_N > 0.06$. The figure shows both the projected points and the fits to the pion valence structure function $F_\pi(x_\pi)$ [Fig. 12(a)] and the nucleon structure function $G_N(x_N)$ [Fig. 12(b)]. The corresponding parameters are given in Table I, column 1. The table also includes results of other analyses discussed below. Tables II and III report the numerical values for the pion and nucleon structure functions. This determination includes no $m^2_{\mu\mu}$ evolution in the parametrization and thus averages over any effect in this interval.

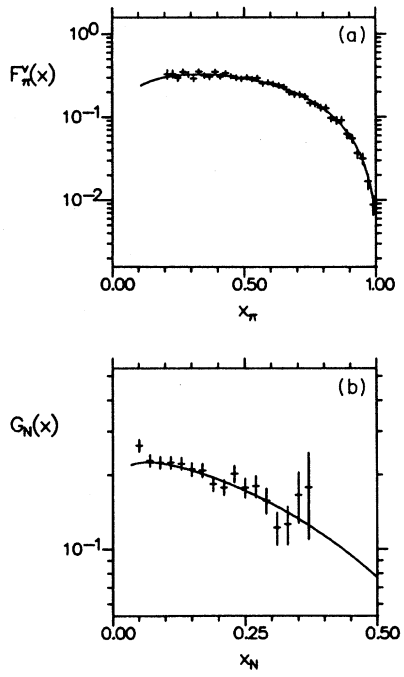

FIG. 12. Results of structure-function fit [$x_N = 0.05$ bins not included in fit or in projection of $F_\pi(x_\pi)$].

Figure 13 shows results for the nucleon structure function in comparison with another μ-pair experiment and with results from deeply inelastic neutrino scattering. The agreement between μ-pair experiments is excellent. The agreement with deeply inelastic scattering helps support the validity of Drell-Yan mechanism.

One should note that the normalization of the nucleon structure function determined here depends on the value used for g_p, the gluon momentum fraction in the nucleon. The value of $g_p=0.48$ from the CCFRR experiment[19] has been used but the error associated with this value leads to a 15% normalization uncertainty in our structure function G_N.

2. *Low-mass anomaly*

Figures 12 and 13 illustrate an interesting effect in the data which occurs at low mass and large Feynman x.

As noted above, the region used for the structure function analysis extends down to $x_N=0.06$ although the cut $M_{\mu\mu}>4.05$ GeV/c^2 allows x_N as low as 0.04. As shown in Figs. 12(b) and 13, the data point here lies several standard deviations above the curve even after inclusion of the 5% systematic error associated with the acceptance. The same trend is seen in the NA3 data[18] shown in Fig. 13 although the error of their closest point in x_N is six times greater. In Figs. 12 and 13 the effect appears as a single point but in x_π-x_N space it corresponds to 11 successive bins 1.5 and 3.3 standard deviations above the fit. This is illustrated in Table IV which shows as a function x_π and x_N the number of standard deviations by which the data depart from the fit. This is the only region in x_π-x_N space which shows a large systematic departure of the data from the fit. The kinematic region in question corresponds to large x_F and low mass where our acceptance is excellent.

There is no evidence from deeply inelastic lepton scattering of a rise in this region of the nucleon structure function and several sets of measurements cover the same kinematic region. If we try to accommodate the data with $x_N<0.06$ by modifying the nucleon structure function, then a value of $\zeta=24\pm3$ is obtained for the nucleon sea exponent. This is to be compared with the result from Abramovicz *et al.*[20] of $\zeta=9$.

Care must be exercised in interpreting such an effect. It does not necessarily follow that it is an anomaly in the

TABLE I. Comparison of structure-function parameters for fits under different conditions but without Q^2 evolution. (1) E615 252 GeV π^-; $x_N>0.06$, (2) E615 252 GeV π^-; $x_N>0.04$, and (3) E615 252 GeV π^-; $x_N>0.04$; $g_\pi=0.37$ assumed.

	E615 (1)[a,b]	E615 (2)[a]	E615 (3)[a]
K	1.75±0.13	1.70±0.07	1.60±0.11
α	0.60±0.03	0.59±0.03	0.66±0.03
β	1.26±0.04	1.25±0.03	1.30±0.04
γ	0.83±0.26	1.31±0.11	0.86±0.23
δ	8.4	8.4	8.4
g_π	0.47	0.47	0.37
μ	0.55±0.06	0.79±0.04	0.55±0.06
ν	2.44±0.40	4.20±0.33	2.46±0.40
ζ	9.0	29±3	9.0
g_p	0.48	0.48	0.48
χ^2/N_{DF}	352/329	369/328	351/329

[a]Errors are statistical only. See text for discussion of systematics.

[b]Correlation matrix:

	K	α	β	γ	μ
α	−0.71				
β	−0.50	0.85			
γ	−0.24	0.37	0.60		
μ	−0.87	0.31	0.14	0.11	
ν	−0.85	0.27	0.13	0.09	0.99

TABLE II. Measured values for the pion valence structure function.

x_π	$F_\pi^v(x_\pi)$
0.21	0.326±0.040
0.23	0.329±0.034
0.25	0.297±0.025
0.27	0.347±0.026
0.29	0.325±0.023
0.31	0.290±0.022
0.33	0.350±0.024
0.35	0.314±0.022
0.37	0.305±0.021
0.39	0.349±0.023
0.41	0.305±0.020
0.43	0.337±0.022
0.45	0.309±0.020
0.47	0.295±0.020
0.49	0.288±0.020
0.51	0.300±0.019
0.53	0.285±0.019
0.55	0.294±0.019
0.57	0.251±0.017
0.59	0.260±0.018
0.61	0.248±0.017
0.63	0.233±0.016
0.65	0.228±0.016
0.67	0.199±0.015
0.69	0.187±0.014
0.71	0.185±0.014
0.73	0.176±0.013
0.75	0.147±0.012
0.77	0.144±0.011
0.79	0.129±0.011
0.81	0.127±0.011
0.83	0.097±0.009
0.85	0.091±0.009
0.87	0.0915±0.0094
0.89	0.0626±0.0073
0.91	0.0550±0.0065
0.93	0.0368±0.0049
0.95	0.0315±0.0046
0.97	0.0168±0.0035
0.99	0.0088±0.0022

TABLE III. Measured values for the nucleon structure function.

x_N	$G_N(x_N)$
0.05	0.263±0.015
0.07	0.228±0.013
0.09	0.224±0.013
0.11	0.224±0.013
0.13	0.222±0.013
0.15	0.210±0.013
0.17	0.208±0.013
0.19	0.183±0.011
0.21	0.177±0.012
0.23	0.202±0.013
0.25	0.177±0.017
0.27	0.180±0.018
0.29	0.157±0.019
0.31	0.122±0.018
0.33	0.126±0.022
0.35	0.166±0.038
0.37	0.178±0.068

nucleon structure function but only that the cross-section excess can most easily be taken up there in the context of the Drell-Yan analysis. What is seen is an excess of events at low mass and $x_F > 0.75$ compared with expectations based on quark structure functions determined over a much larger kinematic interval. The region of the anomaly represents only 3% of the area in x_π-x_N space used for the structure function analysis.

Obviously the effect is just at the edge of the kinematic region used in the present analysis. A full understanding requires extending the analysis to lower masses. There is ample data here and this work is in progress.

Several explanations for the anomaly can be ruled out. One possibility is that there is contamination from the resonances ψ(4030–4415) or from the states ψ(3685) or ψ(3770) because of the detector's finite mass resolution of about 180 MeV/c^2. This seems unlikely since the effect occurs only for $x_F > 0.75$ while the resonance production peaks near $x_F = 0$. Our own analysis of 2.2×10^6 J/ψ events and 3×10^4 ψ(3685) events shows no evidence of a rise in resonance production relative to continuum pro-

TABLE IV. Residuals to structure-function fit. Only the sign is given for magnitudes less than 1.

x_π \ x_N	0.05	0.07	0.09	0.11	0.13	0.15	0.17	0.19	0.21	0.23	0.25	0.27	0.29	0.31	0.33	0.35	0.37
0.21							1.5	-1.4									
0.23						+	-	-									
0.25						-2.0	+	+	-								
0.27					1.5	+	-	+	-	+	+						
0.29					+	-	+	+	+	+	-2.0	+					
0.31					-	-	-1.3	-1.2	-1.3	-1.9	-	-1.4	+				
0.33				1.5	+	-1.2	-	-	1.1	-	1.4	+	-1.6	+			
0.35				-	+	+	-1.5	-2.2	-1.8	-	-	+	-	-	-		
0.37				+	-	-1.5	-	-1.4	-3.4	+	-1.1	+	+	-1.0	+	+	
0.39			1.1	1.6	+	+	1.1	-	-	1.9	-3.6	+	-	-	-3.4	-	-
0.41			-	-1.2	-1.4	-	-	+	+	+	-	-	-	-4.1	-	-1.2	1.2
0.43			+	-	+	+	+	-	-	1.8	+	-1.0	+	-3.0	-	1.6	
0.45			-	-	+	-	+	-1.7	-	1.5	+	1.1	-	-	1.2		
0.47			+	-	-	-	-	-	+	-1.7	+	+	-	+			
0.49			-	-2.0	1.1	+	+	-1.8	-1.2	+	+	1.3	+				
0.51		+	-	+	1.1	+	-	+	-	1.4	1.0	-	-				
0.53		+	-	1.2	-	+	-	-	-	+	-	+					
0.55		1.3	+	+	-	1.1	1.3	-	+	-	+	1.2					
0.57		-	-1.4	+	-	-1.2	-	-	+	+	-						
0.59		-1.2	+	1.0	+	+	-	+	-	1.3	1.5						
0.61		+	-1.2	+	-	+	-	+	-	1.4							
0.63		-	+	+	+	+	-	+	+	+							
0.65		-	+	1.0	+	-	1.2	-	+	-1.2							
0.67		-	-	-2.7	-	-	-	1.9	+								
0.69		-1.4	-	-	+	-1.5	+	1.0	-								
0.71		+	-	-	+	-	+	+	+								
0.73	+	1.1	+	-	-1.3	-	+	+									
0.75	2.0	-	+	-	+	-	-1.5	-2.2									
0.77	+	+	1.4	-	-2.7	-	-	+									
0.79	1.5	+	-1.2	+	-	+	-										
0.81	1.1	1.2	+	-	-2.4	1.4	1.2										
0.83	2.5	-	-	-	-1.8	-	+										
0.85	2.2	+	-1.7	-1.1	+	+	+										
0.87	2.3	-	+	1.0	-	1.6	1.3										
0.89	3.3	-	-1.4	-2.4	+	1.5											
0.91	2.9	+	-	+	+	-1.6											
0.93	2.5	-	-	-1.1	+	+											
0.95	2.3	1.3	1.1	-1.1	+	-2.6											
0.97	2.8	-1.1	+	-1.7	+	+											
0.99	1.6	+	-2.6	1.0	+	-											

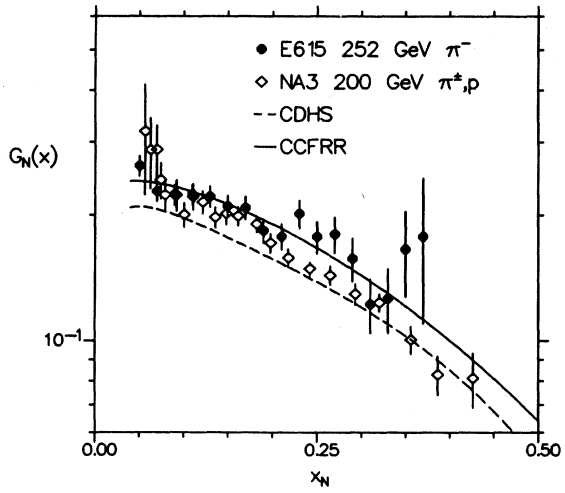

FIG. 13. Comparison of nucleon-structure-function values from this experiment with results from NA3 (Ref. 18) and from deeply inelastic neutrino scattering (Refs. 19 and 20). The normalization is uncertain to ±15% because of uncertainty in the proton's gluon momentum fraction.

duction as x_F increases. Since the branching ratios for ψ(3770–4415) to $\mu^+\mu^-$ are about 10^{-5}, there would have to be at least 20 times more ψ(3770–4415) produced than ψ(3685) to cause the observed excess. This seems unlikely.

The possibility that these muon pairs come from the semileptonic decays of pairs of charmed mesons has been ruled out by simulating the production of $D\bar{D}$ pairs. The resulting mass and x_F distributions do not extend to large enough values to allow such pairs to be reconstructed in the kinematic region in question.

We conclude that the cross-section excess has no simple explanation. To characterize the effect quantitatively Fig. 14 shows the measured cross section versus x_F in several $m_{\mu\mu}$ intervals. The solid line is the cross section expected from the structure-function determination.

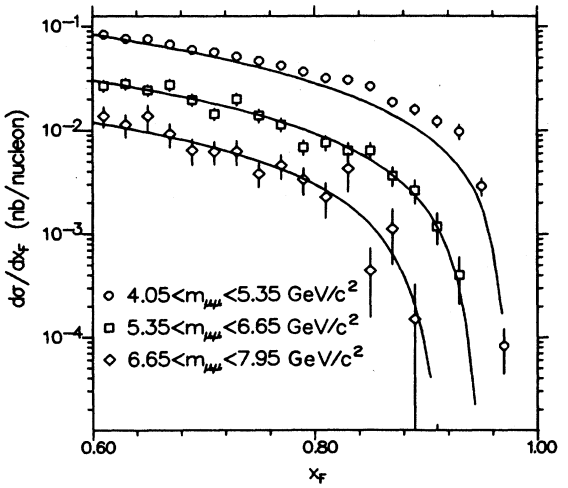

FIG. 14. $d\sigma/dx_F$ in three mass regions, showing curves from Drell-Yan fit to region with $x_N > 0.06$. Excess at low mass corresponds to lowest point in x_N.

3. *Pion structure*

The results for the pion structure function are shown in Fig. 12(a). The parameters corresponding to the curve are given in Table I, column 1 and the projected values for the pion structure function in Table II. The parametrization makes no allowance for scale-breaking effects because these are very small as shown below.

To test the sensitivity of the result to assumptions about the nucleon structure function, we have refit the data while imposing the nucleon results of the CCFRR neutrino experiment (see Appendix D) at a fixed Q^2 of 25 GeV^2. The change is very small, being less than one standard deviation on every point. The main effect is an upward shift in normalization of 2%, and a decrease in the K factor of 10%.

Figure 15 shows a comparison of the measurement given in Fig. 12(a) with Badier *et al.*[18] (NA3) and Betev *et al.*[17] (NA10 Collaboration). The 200-GeV result of NA3 is shown as data points with error bars while the NA10 result appears as a curve because individual points were not reported. As noted above, the normalization requirements of the quark number and momentum densities link the structure function normalization at large x_π to the pion gluon fraction and to the shape of the structure function near $x_\pi = 0$. For the comparison of Fig. 15 we have used a value of $g_\pi = 0.47$; this is the value reported by NA3 and is also used by NA10. The difference in normalization between the experiments is explainable in terms of the different value of α. In this experiment we find $\alpha = 0.6 \pm 0.03$, whereas both NA3 and NA10 report α near 0.4. We found agreement with the 0.4 value only by

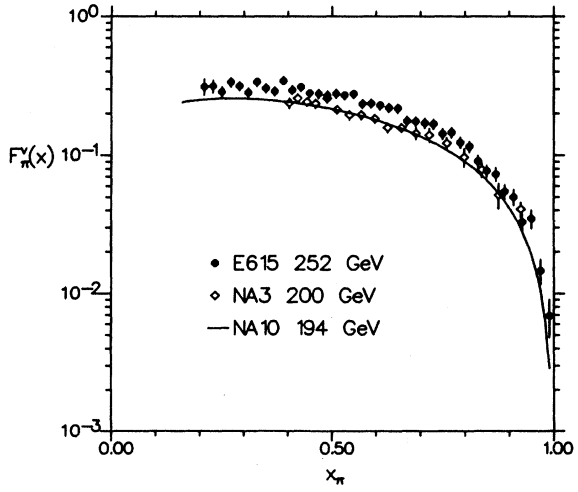

FIG. 15. Comparison of pion-structure-function results with values from NA3 (Ref. 18) and NA10 (Ref. 17). As explained in the text, the normalization for all experiments depends strongly on the structure-function values at low x_π and on the value of g_π.

removing the correction for secondary interactions in the target, which is important at low x_π.

We conclude that the results of this experiment for the shape of the pion structure function above $x_\pi=0.5$ are in good agreement with previous measurements although the overall normalization is higher by $\sim 20\%$. The shape at large x_π is especially well measured here because of the good acceptance for $x_F>0.5$. In a later section the structure function will be examined for scale-breaking effects both in the region $16.4<m_{\mu\mu}^2<73$ $(\mathrm{GeV}/c^2)^2$ and for $m_{\mu\mu}^2>110$ $(\mathrm{GeV}/c^2)^2$.

We next consider the term proportional to γ in the pion-structure-function parametrization. It was introduced to accommodate the higher-twist model of Berger and Brodsky.[8] As discussed in Sec. I, they propose a structure function dependence at large x_π of the form $(1-x_\pi)^2+a/m_{\mu\mu}^2$. A comparison of the structure function points in Fig. 12 or 15 with the proposed form clearly rules out the $(1-x_\pi)^2$ dependence regardless of the value of γ. One might argue that the quadratic term is masked by an additional component not included in the model. To investigate this possibility we have searched for evidence of a nonzero intercept in the pion structure function, that is, a nonzero value of γ.

The first fit in Table I gives a value of $\gamma=0.83\pm0.26$ $(\mathrm{GeV}/c^2)^2$. To better evaluate the significance of this result Fig. 16 shows the results of a fit constraining γ to be zero. Since the significance of a nonzero value for γ is less than 2.5 standard deviations the fit with γ equal zero is only marginally poorer. It should be emphasized that these fits require $x_N>0.06$ to remove the region of the anomaly described above. If instead this region is included, the nucleon sea exponent must be allowed to vary to accommodate the anomaly in the context of the present parametrization. In this case the value $\gamma=1.31\pm0.10$ $(\mathrm{GeV}/c^2)^2$ is obtained with the other parameters reported in Table I, column 2. While the value of γ is statistically very different from zero, the nature of the anomaly needs to be better understood to evaluate the significance of this result.

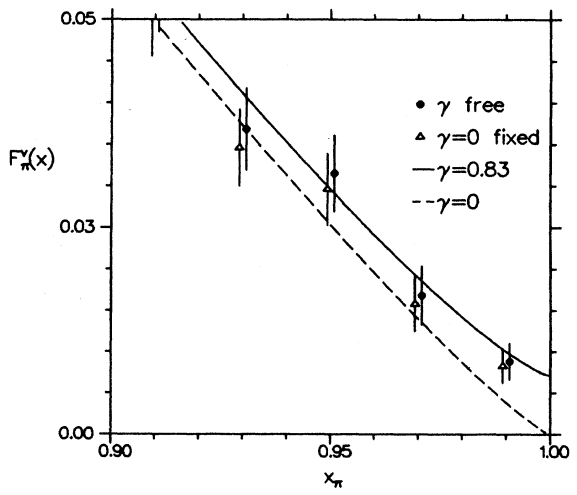

FIG. 16. Comparison of the pion-structure-function results at high x_π with the fit. The solid line and squares correspond to fitting for γ while the dashed line and diamonds correspond to fixing γ at zero.

Another important signature of the higher-twist model is the presence of longitudinal virtual-photon polarization at high x_π. This is discussed in Sec. VI.

In the analysis of the pion structure function, the gluon fraction g_π is taken from Ref. 18. To illustrate the sensitivity of our results for the pion structure function to this parameter the fit was repeated with a value of 0.37 instead of 0.47. The results are given in column 3 of Table I. The largest effect is in the parameter α which changes by two standard deviations.

4. *Scaling and $m_{\mu\mu}^2$ evolution*

The pion and nucleon structure functions are expected to be weak functions of $m_{\mu\mu}^2$. Evolution for the nucleon as a function of Q^2 is well documented in deeply inelastic neutrino and muon scattering[21] but only in muon-pair production can one experimentally address the question of $m_{\mu\mu}^2$ evolution in the pion. In this section we examine the evidence from this experiment for evolution of the pion structure function and compare with results of previous experiments.

Scaling with s. Before searching for $m_{\mu\mu}^2$-dependent changes in the structure functions we wish to assess the consistency of the measured cross sections, as a function of mass, with other experiments. To do this at different beam energies we use the scaling form of the cross section:

$$m_{\mu\mu}^3\frac{d\sigma}{dm_{\mu\mu}}=f(\tau,\bar{s})\ .$$

Scale-breaking effects are expected to be at the level of a few percent for the comparisons made here. Figures 17 and 18 show comparison of this experiment with results from NA3 (Ref. 22) and NA10 (Ref. 17) in the x_F regions reported by these groups. Figure 17 shows excellent agreement with the NA3 result but one sees in Fig. 18, a systematic deviation from NA10 which increases with mass. The NA3 and NA10 data correspond to beam energies of 200 and 194 GeV, respectively, while this experiment is at 252 GeV. Scale breaking is expected to depress values of $m_{\mu\mu}^3 d\sigma/dm_{\mu\mu}$ at fixed $\sqrt{\tau}$, for higher-energy measurements. Thus, the systematic excess compared with NA10 is in the wrong sense to be explained by scaling breaking and will be increased if scale-breaking effects are considered.

$F_\pi^v(x_\pi)$ in different mass regions. As a first test for scale breaking we divide the data into two mass intervals and determine the pion structure function separately in each interval. The lower region is $4.05<M_{\mu\mu}<7.00$ GeV/c^2 and the upper region $7.00<m_{\mu\mu}<8.55$ GeV/c^2. In both cases the nucleon structure function of CCFRR is imposed using a fixed value of $Q^2=\langle m_{\mu\mu}^2\rangle$ corresponding to the mean within the region. The analysis requires $x_N>0.06$ to remove the region related to the

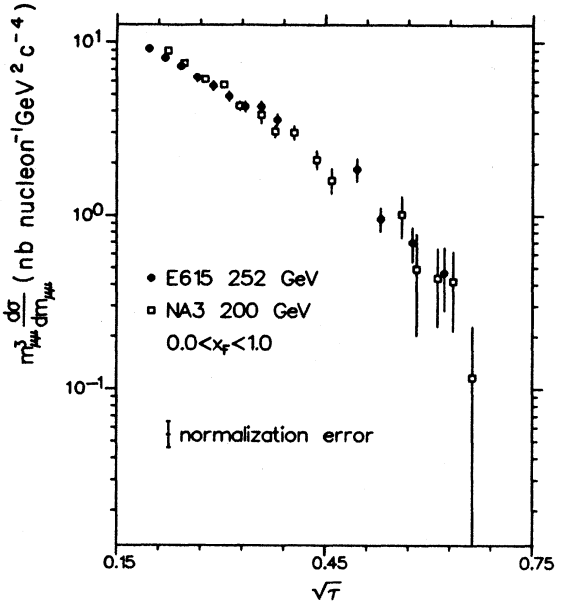

FIG. 17. Comparison of $m^3_{\mu\mu} d\sigma/dm_{\mu\mu}$ from this experiment and NA3 (Ref. 18) for the region $0 < x_F < 1$. Region around the Υ has been excluded.

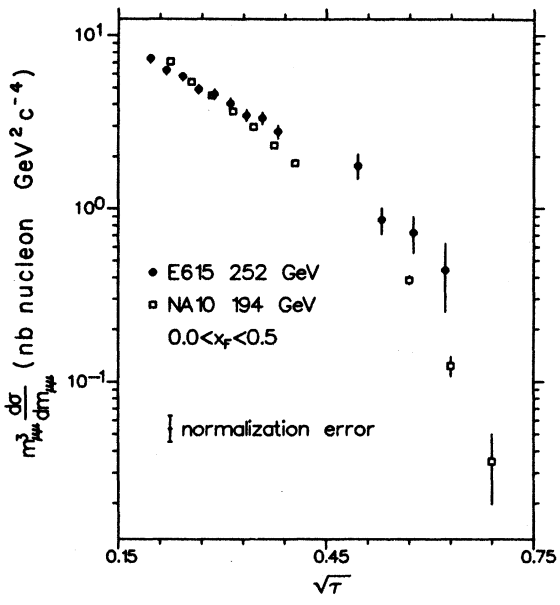

FIG. 18. Comparison of $m^3_{\mu\mu} d\sigma/dm_{\mu\mu}$ from this experiment and NA10 (Ref. 17) for the region $0 < x_F < 0.5$. Region around Υ has been excluded.

anomaly discussed above. The resulting structure functions are displayed in Fig. 19 and the parameters from the fits given in Table V, columns 1 and 2.

Scale breaking is expected to steepen the structure function at high x for higher-mass data. The values of the parameter β are 1.29 ± 0.23 from the higher-mass region and 1.27 ± 0.04 from the lower-mass region. As one can see from Fig. 19 there is no evidence for scale breaking within the level of sensitivity of this test. Using the Buras-Gaemers parametrization described above, one expects the value of β to vary by 0.06 and these results are consistent with that. Appreciably larger scale breaking can be ruled out.

$m^2_{\mu\mu}$-evolved fit. A second method of searching for scaling breaking is to compare the goodness of fit for parametrizations that incorporate scale breaking with ones which do not. It is important to realize, as described above, that no additional independent parameters are introduced in allowing for scale breaking. Thus, an improvement in the χ^2 confidence level would be at least circumstantial evidence of $m^2_{\mu\mu}$ dependence of the structure function. In this analysis, the Q-evolution of the pion structure function follows the prescription described in Sec. IV A 3 using $\Lambda = 150$ MeV.

Table V, columns 3 and 4, give the fit results with and without Q^2 evolution. The χ^2 confidence levels are 49% and 39%; both excellent fits. Thus, in this region the evolved and nonevolved forms describe the data well. The main effect of Q^2 evolution enters at high mass, as we see below.

x_F dependence of the cross section. Figure 20 shows our measurements of $d\sigma/dx_F d\sqrt{\tau}$ as a function of x_F for five $\sqrt{\tau}$ intervals. Corresponding numerical values appear in Table VI. The highest $\sqrt{\tau}$ interval corresponds to the re-

TABLE V. Results of fits for the pion structure-function parameters, allowing for Q^2 evolution. (1) $x_N > 0.06$; $4.05 < m_{\mu\mu} < 7.0$ GeV; CCFRR nucleon (Q^2 fixed); no π evol., (2) $x_N > 0.06$; $7.0 < m_{\mu\mu} < 8.55$ GeV; CCFRR nucleon (Q^2 fixed); no π evol., (3) $x_N > 0.06$; $4.05 < m_{\mu\mu} < 8.55$ GeV; CCFRR nucleon (Q^2 fixed); no π evol., (4) $x_N > 0.06$; $4.05 < m_{\mu\mu} < 8.55$ GeV; CCFRR nucleon (Q^2 evol.); evolving π, and (5) NA10 194 GeV π^-; CDHS nucleon parameters; evolving pion (LLA).

	E615 (1)[a]	E615 (2)[a]	E615 (3)[a]	E615 (4)[a]	NA10 (5)
K	1.78±0.07	1.48±0.5	1.77±0.06	1.80±0.06	2.33±0.10
α	0.572±0.03	0.78±0.34	0.58±0.03	0.56±0.03	0.40±0.03
β	1.266±0.04	1.29±0.23	1.26±0.03	1.21±0.03	0.96±0.04
γ	0.78±0.27	1.08±1.8	0.76±0.24	0.63±0.22	
δ	8.4	8.4	8.4	8.4	8.4
g_π	0.47	0.47	0.47	0.47	0.47
χ^2/N_{DF}	161/187	122/96	332/331	338/331	

[a]Errors are statistical only. See text for discussion of systematics.

TABLE VI. Measured differential cross section in x_F and $\sqrt{\tau}$.

$\sqrt{\tau}$		x_F		$d\sigma/dx_F d\sqrt{\tau}$
Low	High	Low	High	(nb/nucleon)
0.185	0.208	0.00	0.10	4.66±0.32
0.185	0.208	0.10	0.20	4.73±0.29
0.185	0.208	0.20	0.30	4.79±0.28
0.185	0.208	0.30	0.40	3.76±0.22
0.185	0.208	0.40	0.50	3.12±0.18
0.185	0.208	0.50	0.60	2.12±0.12
0.185	0.208	0.60	0.70	1.56±0.13
0.208	0.231	−0.10	0.00	2.40±0.23
0.208	0.231	0.00	0.10	2.86±0.21
0.208	0.231	0.10	0.20	2.77±0.19
0.208	0.231	0.20	0.30	2.68±0.17
0.208	0.231	0.30	0.40	2.13±0.13
0.208	0.231	0.40	0.50	1.77±0.11
0.208	0.231	0.50	0.60	1.44±0.09
0.208	0.231	0.60	0.70	0.95±0.06
0.208	0.231	0.70	0.80	0.69±0.05
0.208	0.231	0.80	0.90	0.33±0.08
0.231	0.254	−0.10	0.00	1.642±0.164
0.231	0.254	0.00	0.10	1.787±0.149
0.231	0.254	0.10	0.20	1.660±0.128
0.231	0.254	0.20	0.30	1.718±0.122
0.231	0.254	0.30	0.40	1.549±0.106
0.231	0.254	0.40	0.50	1.331±0.090
0.231	0.254	0.50	0.60	0.931±0.064
0.231	0.254	0.60	0.70	0.735±0.049
0.231	0.254	0.70	0.80	0.350±0.026
0.231	0.254	0.80	0.90	0.158±0.014
0.231	0.254	0.90	1.00	0.010±0.004
0.254	0.277	−0.20	−0.10	0.763±0.124
0.254	0.277	−0.10	0.00	1.075±0.128
0.254	0.277	0.00	0.10	1.011±0.100
0.254	0.277	0.10	0.20	1.024±0.091
0.254	0.277	0.20	0.30	1.192±0.096
0.254	0.277	0.30	0.40	1.027±0.080
0.254	0.277	0.40	0.50	0.839±0.065
0.254	0.277	0.50	0.60	0.626±0.050
0.254	0.277	0.60	0.70	0.444±0.035
0.254	0.277	0.70	0.80	0.241±0.021
0.254	0.277	0.80	0.90	0.105±0.012
0.254	0.277	0.90	1.00	0.010±0.003
0.277	0.300	−0.10	0.00	0.722±0.121
0.277	0.300	0.00	0.10	0.863±0.115
0.277	0.300	0.10	0.20	0.892±0.102
0.277	0.300	0.20	0.30	0.660±0.076
0.277	0.300	0.30	0.40	0.694±0.071
0.277	0.300	0.40	0.50	0.639±0.061
0.277	0.300	0.50	0.60	0.458±0.046
0.277	0.300	0.60	0.70	0.300±0.030
0.277	0.300	0.70	0.80	0.153±0.017
0.277	0.300	0.80	0.90	0.058±0.009
0.277	0.300	0.90	1.00	0.001±0.001
0.300	0.323	−0.20	−0.10	0.310±0.081
0.300	0.323	−0.10	0.00	0.429±0.075
0.300	0.323	0.00	0.10	0.608±0.081
0.300	0.323	0.10	0.20	0.497±0.063
0.300	0.323	0.20	0.30	0.638±0.074
0.300	0.323	0.30	0.40	0.513±0.057

TABLE VI. (*Continued*).

$\sqrt{\tau}$		x_F		$d\sigma/dx_F d\sqrt{\tau}$
Low	High	Low	High	(nb/nucleon)
0.300	0.323	0.40	0.50	0.424±0.048
0.300	0.323	0.50	0.60	0.297±0.037
0.300	0.323	0.60	0.70	0.183±0.024
0.300	0.323	0.70	0.80	0.101±0.014
0.300	0.323	0.80	0.90	0.039±0.008
0.323	0.346	−0.20	−0.10	0.388±0.087
0.323	0.346	−0.10	0.00	0.281±0.057
0.323	0.346	0.00	0.10	0.366±0.055
0.323	0.346	0.10	0.20	0.400±0.052
0.323	0.346	0.20	0.30	0.415±0.049
0.323	0.346	0.30	0.40	0.321±0.040
0.323	0.346	0.40	0.50	0.290±0.036
0.323	0.346	0.50	0.60	0.188±0.027
0.323	0.346	0.60	0.70	0.141±0.022
0.323	0.346	0.70	0.80	0.089±0.015
0.323	0.346	0.80	0.90	0.015±0.005
0.346	0.369	−0.20	−0.10	0.181±0.051
0.346	0.369	−0.10	0.00	0.200±0.044
0.346	0.369	0.00	0.10	0.212±0.037
0.346	0.369	0.10	0.20	0.237±0.036
0.346	0.369	0.20	0.30	0.331±0.045
0.346	0.369	0.30	0.40	0.277±0.037
0.346	0.369	0.40	0.50	0.279±0.035
0.346	0.369	0.50	0.60	0.170±0.025
0.346	0.369	0.60	0.70	0.117±0.019
0.346	0.369	0.70	0.80	0.075±0.014
0.346	0.369	0.80	0.90	0.014±0.005
0.369	0.392	−0.20	−0.10	0.073±0.035
0.369	0.392	−0.10	0.00	0.164±0.043
0.369	0.392	0.00	0.10	0.191±0.038
0.369	0.392	0.10	0.20	0.232±0.037
0.369	0.392	0.20	0.30	0.214±0.033
0.369	0.392	0.30	0.40	0.225±0.034
0.369	0.392	0.40	0.50	0.134±0.022
0.369	0.392	0.50	0.60	0.116±0.020
0.369	0.392	0.60	0.70	0.100±0.019
0.369	0.392	0.70	0.80	0.045±0.011
0.369	0.392	0.80	0.90	0.005±0.003
0.392	0.415	−0.10	0.00	0.069±0.026
0.392	0.415	0.00	0.10	0.131±0.032
0.392	0.415	0.10	0.20	0.160±0.029
0.392	0.415	0.20	0.30	0.154±0.028
0.392	0.415	0.30	0.40	0.151±0.026
0.392	0.415	0.40	0.50	0.125±0.022
0.392	0.415	0.50	0.60	0.113±0.022
0.392	0.415	0.60	0.70	0.060±0.013
0.392	0.415	0.70	0.80	0.031±0.009
0.392	0.415	0.80	0.90	0.003±0.002
0.415	0.438	−0.20	−0.10	0.157±0.069
0.415	0.438	−0.10	0.00	0.099±0.034
0.415	0.438	0.00	0.10	0.188±0.039
0.415	0.438	0.10	0.20	0.141±0.028
0.415	0.438	0.20	0.30	0.217±0.035
0.415	0.438	0.30	0.40	0.151±0.026
0.415	0.438	0.40	0.50	0.156±0.026
0.415	0.438	0.50	0.60	0.132±0.024
0.415	0.438	0.60	0.70	0.078±0.019
0.415	0.438	0.70	0.80	0.014±0.006

TABLE VI. (*Continued*).

$\sqrt{\tau}$		x_F		$d\sigma/dx_F d\sqrt{\tau}$
Low	High	Low	High	(nb/nucleon)
0.438	0.461	−0.10	0.00	0.129±0.059
0.438	0.461	0.00	0.10	0.088±0.027
0.438	0.461	0.10	0.20	0.064±0.018
0.438	0.461	0.20	0.30	0.113±0.024
0.438	0.461	0.30	0.40	0.117±0.025
0.438	0.461	0.40	0.50	0.095±0.020
0.438	0.461	0.50	0.60	0.084±0.020
0.438	0.461	0.60	0.70	0.035±0.010
0.438	0.461	0.70	0.80	0.009±0.005
0.461	0.484	−0.10	0.00	0.073±0.035
0.461	0.484	0.00	0.10	0.049±0.018
0.461	0.484	0.10	0.20	0.089±0.026
0.461	0.484	0.20	0.30	0.101±0.025
0.461	0.484	0.30	0.40	0.079±0.017
0.461	0.484	0.40	0.50	0.066±0.018
0.461	0.484	0.50	0.60	0.052±0.015
0.461	0.484	0.60	0.70	0.017±0.008
0.461	0.484	0.70	0.80	0.010±0.007
0.484	0.507	−0.10	0.00	0.0114±0.0118
0.484	0.507	0.00	0.10	0.0289±0.0156
0.484	0.507	0.10	0.20	0.0853±0.0280
0.484	0.507	0.20	0.30	0.0352±0.0129
0.484	0.507	0.30	0.40	0.0879±0.0270
0.484	0.507	0.40	0.50	0.0378±0.0132
0.484	0.507	0.50	0.60	0.0134±0.0065
0.484	0.507	0.60	0.70	0.0107±0.0069
0.507	0.530	0.00	0.10	0.0308±0.0200
0.507	0.530	0.10	0.20	0.0697±0.0261
0.507	0.530	0.20	0.30	0.0271±0.0122
0.507	0.530	0.30	0.40	0.0218±0.0097
0.507	0.530	0.40	0.50	0.0208±0.0088
0.507	0.530	0.50	0.60	0.0099±0.0054
0.507	0.530	0.60	0.70	0.0090±0.0061
0.530	0.553	−0.10	0.00	0.0142±0.0153
0.530	0.553	0.00	0.10	0.0109±0.0115
0.530	0.553	0.10	0.20	0.0057±0.0058
0.530	0.553	0.20	0.30	0.0060±0.0062
0.530	0.553	0.30	0.40	0.0173±0.0078
0.530	0.553	0.40	0.50	0.0128±0.0081
0.530	0.553	0.50	0.60	0.0047±0.0035
0.530	0.553	0.60	0.70	0.0055±0.0045
0.553	0.576	0.00	0.10	0.0307±0.0212
0.553	0.576	0.10	0.20	0.0179±0.0140
0.553	0.576	0.20	0.30	0.0111±0.0084
0.553	0.576	0.30	0.40	0.0052±0.0054
0.553	0.576	0.40	0.50	0.0120±0.0067
0.553	0.576	0.50	0.60	0.0028±0.0029
0.576	0.599	0.00	0.10	0.0141±0.0158
0.576	0.599	0.10	0.20	0.0220±0.0184
0.576	0.599	0.20	0.30	0.0139±0.0112
0.576	0.599	0.30	0.40	0.0141±0.0094
0.576	0.599	0.40	0.50	0.0252±0.0170
0.576	0.599	0.50	0.60	0.0024±0.0025

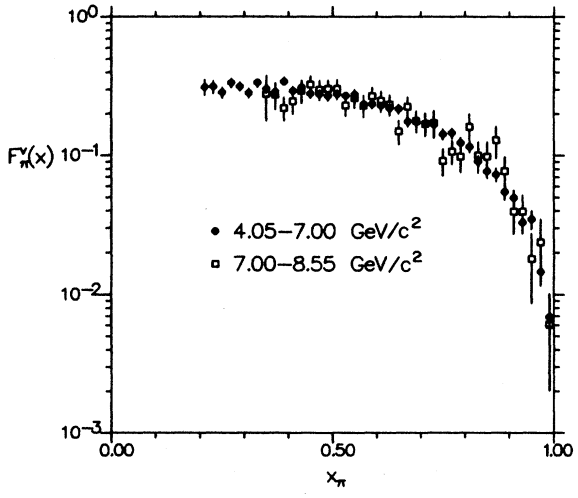

FIG. 19. Comparison of $F_\pi^v(x_\pi)$ in two regions of $m_{\mu\mu}$. The corresponding fit parameters are given in Table V. The higher-mass data have been normalized to the lower-mass points to facilitate comparison.

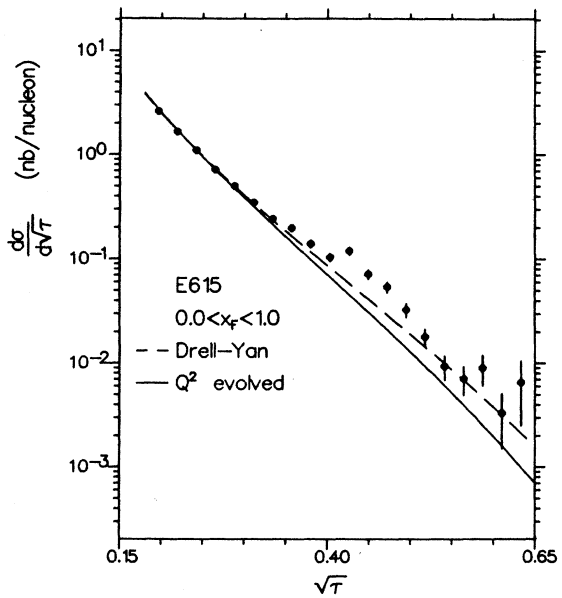

FIG. 21. Result from this experiment on $d\sigma/d\sqrt{\tau}$; curves are from fits (3) and (4) in Table V with fit K factors.

gion above the Υ. In Fig. 20 the solid curve is the QCD expectation in leading-log approximation with $\Lambda = 150$ MeV. The absolute normalization is set independently in each $\sqrt{\tau}$ interval using the K-factor values discussed below. The shape of the last curve depends mainly on our measurements at masses below the Υ and the data are consistent with this extrapolation. Scale-breaking effects reflect mainly in the overall normalization of these $\sqrt{\tau}$ intervals and are not apparent in the shape at the present level of statistics.

$\sqrt{\tau}$ dependence of K factor. Figure 21 shows the $\sqrt{\tau}$ dependence of the measured cross section, integrated over $x_F > 0$. The curves correspond to Drell-Yan and leading-log approximations to the cross section, as fit to

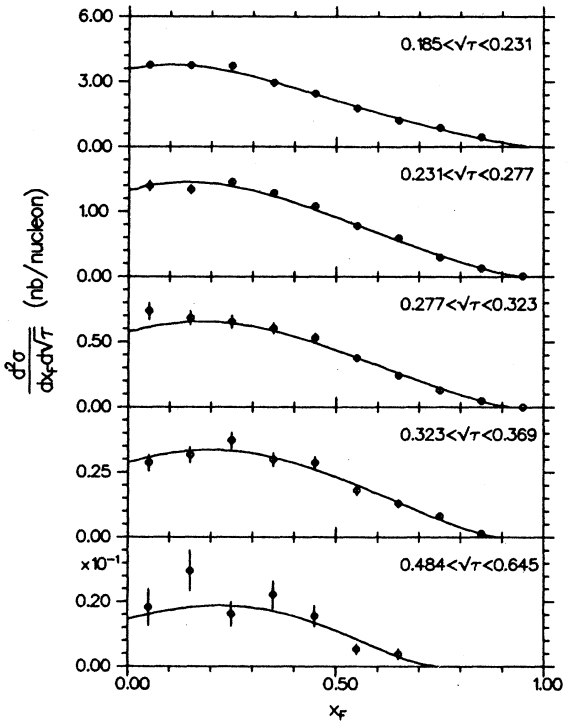

FIG. 20. Results from this experiment on $d^2\sigma/dx_F d\sqrt{\tau}$; curves are from fit (4) in Table V with Q^2 evolution. Curves have been scaled by K factors corresponding to those in Fig. 22.

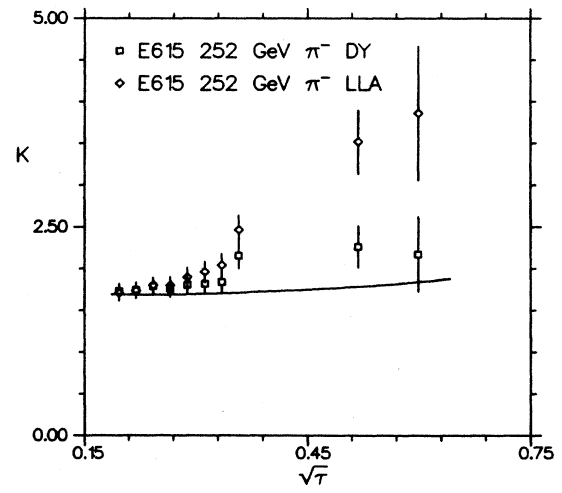

FIG. 22. K factor as a function of $\sqrt{\tau}$ from this experiment relative to naive Drell-Yan and a leading-log-evolved fit. Table VII shows the effect on K of various systematic uncertainties. These tend to produce an overall scale change and are not reflected in the error bars shown. The solid curve shows the K factor from a first-order α_s calculation (Ref. 6), relative to the leading-log cross section.

TABLE VII. Sensitivity of K to systematic uncertainties.

Source	Orig. value	Test value	ΔK (%)
Integrated luminosity			±15
Reinteraction correction		±20%	±5
g_π	0.47±0.15[a]	0.32	−15
g_p	0.48[b]	0.40	−10
δ	8.4±2.5[a]	6.0	−11
ζ	9.0[b]	8.5	+2

[a]From NA3, Ref. 18.
[b]From CCFRR, Ref, 19.

the data in the region $4.05 < m_{\mu\mu} < 8.55$ GeV/c^2. The fit parameters are reported in columns 3 and 4 of Table V. The data of Fig. 21 clearly lie above the expected level for the evolved fit.

We have searched for instrumental effects which could produce this result. The accidental background falls more steeply with mass than the data and is negligible for the region in question. For the 156 events above the Υ, the angular distributions and the distributions of track impact points on various detector planes are in good agreement with Monte Carlo predictions and suggest no evidence for background. The kinematic distributions for these events are also well modeled in the simulation.

The cross-section excess can be characterized by a K-factor depending on $\sqrt{\tau}$. Figure 22 shows the K factor as a function of $\sqrt{\tau}$, with respect to both the pure Drell-Yan cross section and the leading-log approximation. The errors shown are only statistical. Table VII lists sources of systematic errors. These include uncertainties in the integrated luminosity, in corrections for secondary interactions and in parameters characterizing the unmeasured low-x part of the structure functions. When added in quadrature these give an overall systematic error of 26%.

The NA3 Collaboration[18] have reported a value $K = 2.3 \pm 0.5$ averaged over the interval $0.22 < \sqrt{\tau} < 0.44$. This is to be compared with 1.9±0.5 determined from this experiment over the same interval and including systematic errors. The two results are in good agreement.

We have checked that the K-factor values from our data are insensitive to the form used for the nucleon structure function. The same result is obtained using our own nucleon structure function or the results from CCFRR.

The result for K at large $\sqrt{\tau}$ are sensitive to the value of Λ. In this analysis is $\Lambda = 0.15$ GeV has been used.[23] A larger value would increase the size of any cross-section excess at large $\sqrt{\tau}$.

V. TRANSVERSE-MOMENTUM DISTRIBUTION

A. Introduction

Previous experiments have observed that the transverse momenta of Drell-Yan pairs has a mean value $\langle p_T \rangle > 1$ GeV/c and varies with $\sqrt{s}$ (Ref. 16). This figure is substantially larger than the few hundred MeV/c characteristic of an intrinsic p_T from quark confinement. The excess is believed to arise from QCD effects involving additional gluons in the initial or final state. The Feynman diagrams of these processes were shown in Fig. 3. Their contribution to the p_T spectra have been calculated, with the divergence at $p_T = 0$ regularized using the intrinsic quark transverse momentum.[24]

B. Parametrization and analysis method

We characterize the p_T dependence of our data by a function $P(p_T; x_F, m_{\mu\mu})$ such that

$$\frac{d^3\sigma}{dx_\pi dx_N dp_T} = \frac{d^2\sigma_{\rm DY}}{dx_\pi dx_N} P(p_T; x_F, m_{\mu\mu}) .$$

For convenient normalization we require that

$$\int dp_T P(p_T; x_F, m_{\mu\mu}) = 1 .$$

The form chosen for the function P is completely empirical; we write

$$P(p_T; x_F, m_{\mu\mu}) = \frac{5\frac{a}{b}\left[\frac{p_T}{b}\right]^{a-1}}{[1+(p_T/b)^a]^6} ,$$

where $a \equiv a(x_F, m_{\mu\mu})$ and $b \equiv b(x_F, m_{\mu\mu})$. This implies that

$$\langle p_T^2 \rangle = \frac{2b^2}{a} B(2/a, 5-2/a)$$

for any x_F and $m_{\mu\mu}$, where $B(x,y)$ is the Euler beta function. This *ad hoc* parametrization is found to describe the distribution quite well over the measured kinematic range.

To determine the parameters a and b, the bin contents were corrected for acceptance and background and then divided into regions of p_T, x_F, and $m_{\mu\mu}$. In each interval of x_F and $m_{\mu\mu}$, the p_T spectrum was fit to the above form. To minimize the background subtraction, a requirement of $|\cos\theta| < 0.85$ was applied to the data. This eliminates almost all the halo-associated background shown in Fig. 9. After this cut the background subtraction is negligible over the full p_T range reported here. The small loss of data from the cut was compensated in the acceptance calculation. No requirement was made on x_N for this analysis. Figure 23 shows the measured p_T spectrum, integrated over the indicated intervals of mass and x_F, and the parametrized variation.

C. Results

The parameters a and b were found to vary smoothly over the x_F and $m_{\mu\mu}$ regions reported below. There is no significant correlation between them. Their values as a function of x_F and $m_{\mu\mu}$ are given in Appendix A.

Figure 24 shows the variation of $\langle p_T^2 \rangle$ as a function of x_F. There is a very significant drop at high x_F. The individual p_T spectra for x_F intervals of 0.1 are shown in Fig.

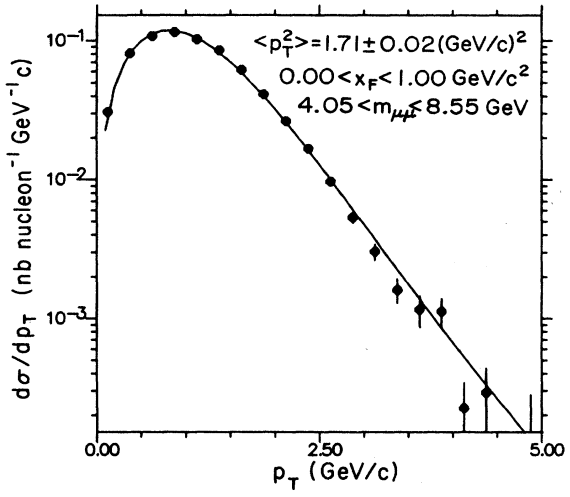

FIG. 23. p_T spectrum corrected for acceptance. The background, as estimated from random pairings, is negligible.

25 together with the parametrized fit. As can be seen, the quality of the fit is excellent.

Spectra integrated over the range $0 < x_F < 1$ have also been obtained in various regions of $m_{\mu\mu}$. Figures 26 and 27 show $\langle p_T^2 \rangle$, and p_T spectra as a function of $m_{\mu\mu}$. Note especially the drop in $\langle p_T^2 \rangle$ in the mass region of the upsilon resonances. This indicates a clear change in the production mechanism for this interval. The results for $\langle p_T^2 \rangle$ vs $m_{\mu\mu}$ indicate a slow increase in p_T as $m_{\mu\mu}$ grows. Since this parameter is integrated over all x_F it is quite insensitive to the small-cross-section region at high x_F.

A comparison with other experiments is given in Fig. 28, where $\langle p_T^2 \rangle$ in the region $x_F > 0$ is plotted as a function of s for the same value of $\sqrt{\tau}=0.28$ (Ref. 16). The results from this experiment agree with the general increase with s. This trend is predicted by QCD calculations but as noted by Malhotra,[16] the QCD calculations fail to explain the magnitude of the increase in $\langle p_T^2 \rangle$ with s. The QCD prediction for $\langle p_T^2 \rangle$ falls 60% too low at

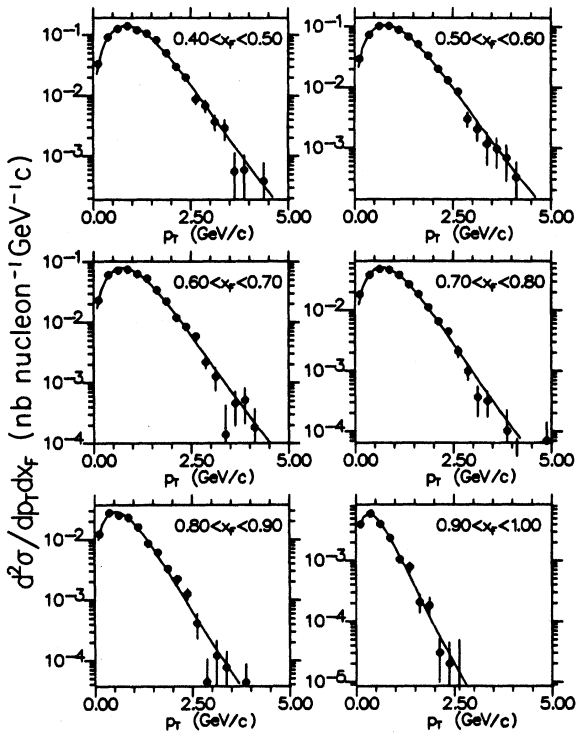

FIG. 25. $d\sigma/dp_T$ for $4.05 < m_{\mu\mu} < 8.55$ GeV/c^2, in regions of x_F; curves are result of fits.

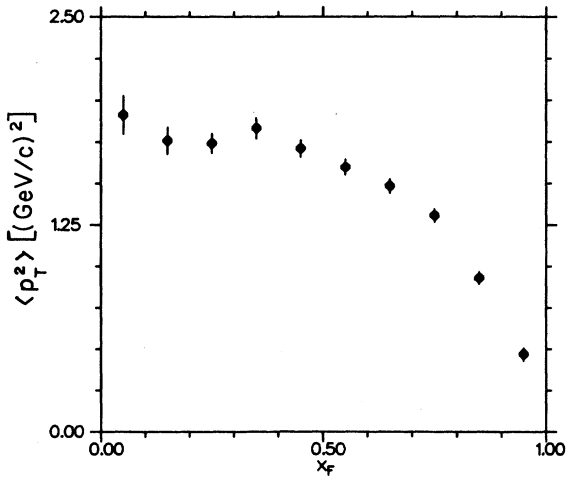

FIG. 24. Mean p_T^2 for $4.05 < m_{\mu\mu} < 8.55$ GeV/c^2, as a function of x_F. The values are those obtained from the fitted form.

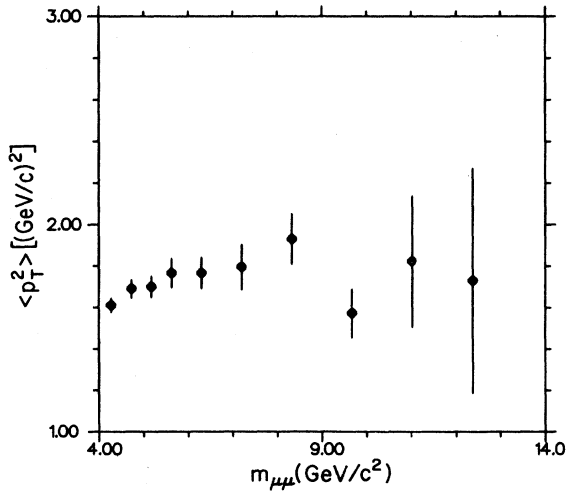

FIG. 26. Fit results for $0 < x_F < 1$, in regions of $m_{\mu\mu}$ showing inferred values for $\langle p_T^2 \rangle$ vs $m_{\mu\mu}$. Region near Υ shows lower value of $\langle p_T^2 \rangle$.

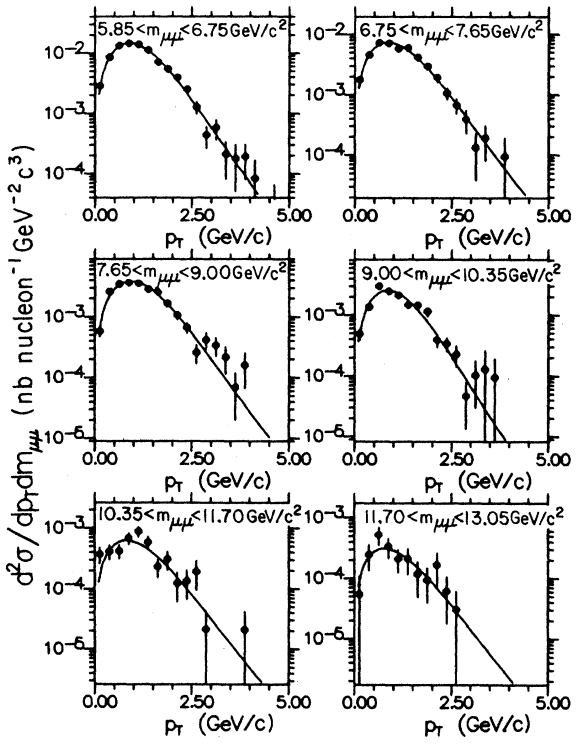

FIG. 27. $d\sigma/dp_T$ for $0<x_F<1$, in regions of $m_{\mu\mu}$.

$s=500$ GeV^2.

The results for $\langle p_T^2 \rangle$ as a function of longitudinal momentum are compared with other experiments in Fig. 29. Here the pseudorapidity $y \equiv \frac{1}{2}\ln(x_\pi/x_N)$ is used since this is the form available from earlier work.[16,25] The results shown in Fig. 29 for the three experiments agree fairly well and some of the spread may be due to different beam energies.

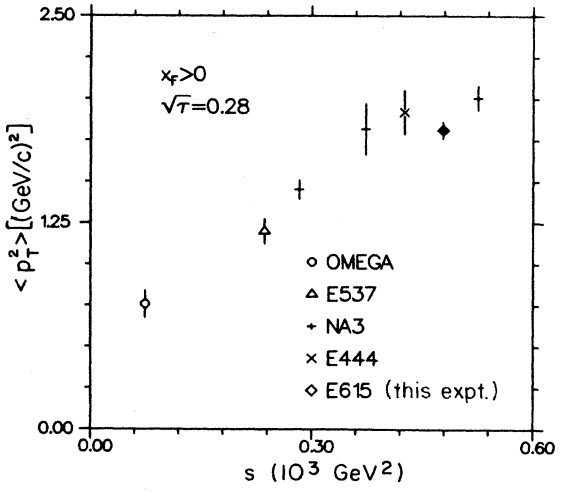

FIG. 28. $\langle p_T^2 \rangle$ vs s for different experiments (Ref. 16).

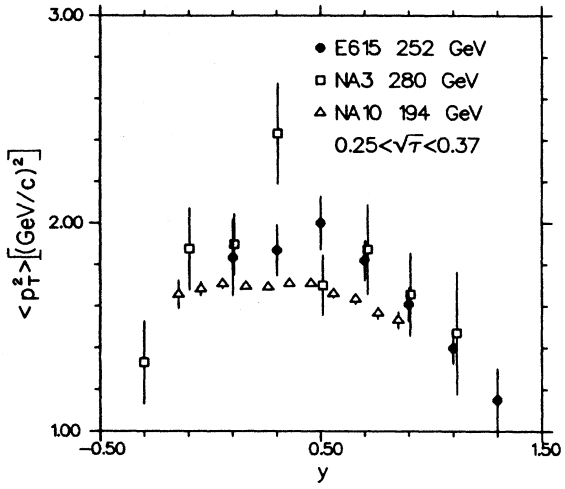

FIG. 29. $\langle p_T^2 \rangle$ vs y for different experiments (Refs. 16 and 25). Note that the experiments are at different beam energies and a growth of $\langle p_T^2 \rangle$ with energy is shown in Fig. 28.

Figure 30 compares the change in $\langle p_T^2 \rangle$ with $\sqrt{\tau}$ as seen in the same three experiments, although in somewhat different y intervals. A slow increase in $\langle p_T^2 \rangle$ with $\sqrt{\tau}$ is seen in each case for the mass range below the Υ. There is the indication from the NA10 data[25] that $\langle p_T^2 \rangle$ decreases above the Υ but the statistics of this work are insufficient to confirm it.

VI. ANGULAR DISTRIBUTIONS

A. Parametrization and analysis method

The most general form of the dimuon angular distributions, assuming a $J^P=1^-$ state, is

$$\frac{1}{\sigma}\frac{d^2\sigma}{d\Omega}=\frac{3}{4\pi(\lambda+3)}\left[1+\lambda\cos^2\theta+\mu\sin 2\theta\cos\phi+\frac{\nu}{2}\sin^2\theta\cos 2\phi\right],$$

where λ, μ, and ν are functions of the kinematic variables $m_{\mu\mu}$, x_π, and p_T (Ref. 5).

The variables $\cos\theta$ and ϕ are defined in the muon-pair rest system with respect to particular reference directions. The three reference frames used here are the t-channel, or Gottfried-Jackson (GJ) frame, the Collins-Soper (CS) frame, and the u-channel (UC) frame. Their definitions were given in Sec. I. They differ only by a rotation about the axis perpendicular to the plane formed by the pion and nucleon directions in the mu-pair rest system. Given the coefficients λ, μ, ν in one frame they can be calculated in another by the procedure given in Appendix E.

In the analysis described below we explore the dependence of λ, μ, ν on $m_{\mu\mu}$, x_π, and p_T, one variable at a time, integrating over the other two. In general, the data were divided into a uniform grid 10×10 cells over the

full physical range of $\cos\theta$ and ϕ. In some cases near the edge of phase space where there were few events a 5×5 grid was used. Cells with acceptance less than 0.75% were eliminated. These lie in the region with $\cos\theta$ near -1 and ϕ near π, or $\cos\theta$ near $+1$ and ϕ near 0. To minimize the background subtraction we eliminated the region $|\cos\theta|>0.9$. These cuts together eliminate about one quarter of the bins but only a few percent of the data.

The results for the angular distributions depend on the calculated acceptance correction for the detector. A major effort was made to eliminate systematic errors in this correction. The measured correlation between incident beam angle, position on the target, and momentum was included in the detector simulation. As described in Sec. II D the efficiency of each scintillation counter was examined as a function of position on the counter and the small inefficiencies were included in the acceptance calculation. The errors on the results reported below reflect a component associated with residual systematic effects.

B. Results

1. *Overview of results*

Figure 31 shows the projected $\cos\theta$ distribution for six regions of x_π with $4.05<m_{\mu\mu}<4.95$ GeV/c^2. The corresponding values of λ are plotted in Fig. 32 as a function of x_π. The values of λ are close to 1 except for the highest value of x_π. This latter result is essentially unchanged if one eliminates the point in Fig. 31 with $\cos\theta<-0.6$ and $x_\pi>0.92$. The background subtraction is the largest here, as can be seen from Fig. 9. The curves in Fig. 32 will be discussed below in VI B 3.

The presence of the ν term in the angular distribution is most easily demonstrated from the variation with ϕ for the region $|\cos\theta|<0.6$. In this interval the contribution of the μ term integrates to zero. Figure 33 shows the ϕ

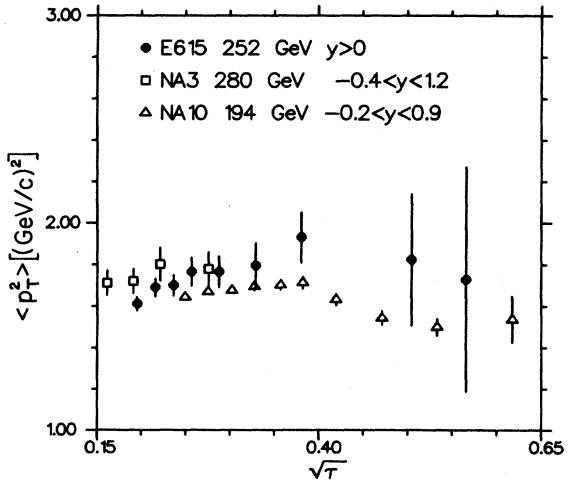

FIG. 30. $\langle p_T^2\rangle$ vs $\sqrt{\tau}$ for different experiments (Refs. 16 and 25). (Note different beam energies.)

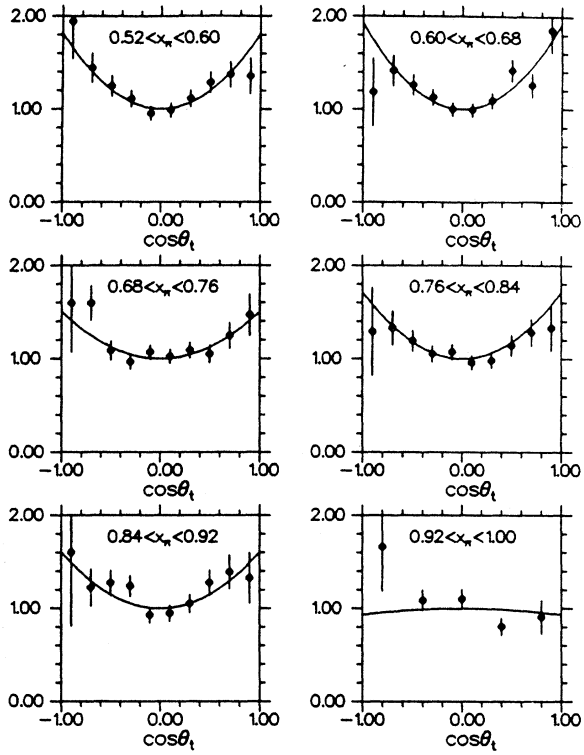

FIG. 31. Result for GJ $\cos\theta$ distributions in regions of x_π for $4.05<m_{\mu\mu}<4.95$ GeV/c^2. Curves are from fit to $\cos\theta$-ϕ plane.

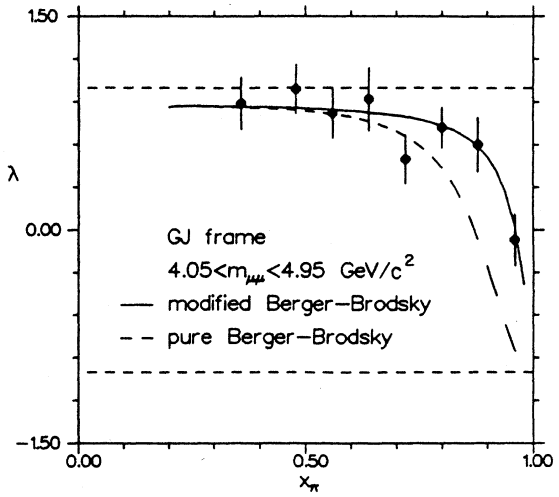

FIG. 32. λ vs x_π for the mass region $4.05<m_{\mu\mu}<4.95$ GeV/c^2 showing curves from high-twist predictions (Ref. 8) with $\langle k_T^2\rangle=0.8$ (GeV/c)^2. The solid line corresponds to the measured shape of the pion structure function while the dashed line corresponds to the predicted $(1-x_\pi)^2$ shape.

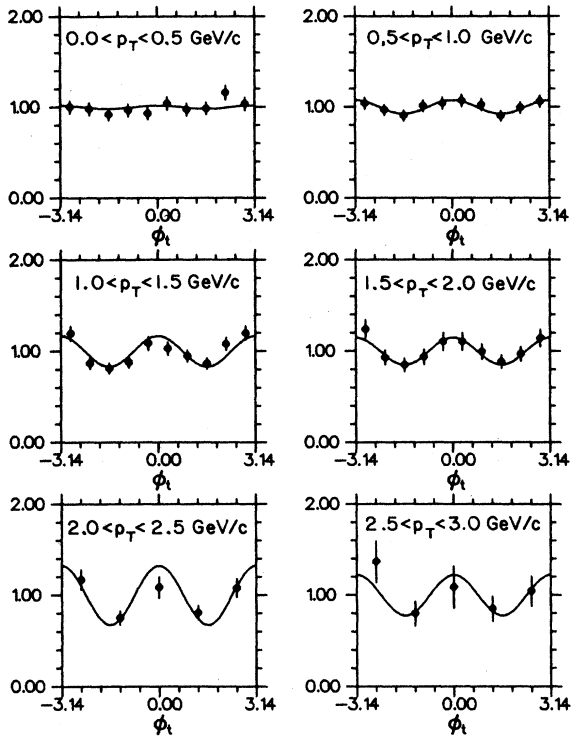

FIG. 33. Result for GJ ϕ distributions integrated over the range $-0.6<\cos\theta<0.6$ in regions of p_T for $4.05<m_{\mu\mu}<8.55$ GeV/c^2. Curves are from fit to $\cos\theta$-ϕ plane.

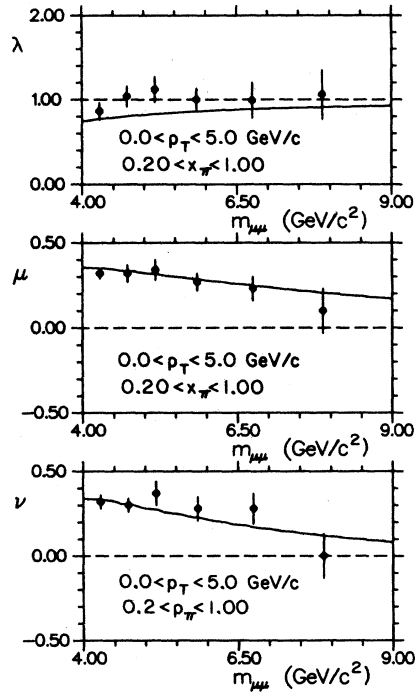

FIG. 35. Result for λ, μ, and ν as a function of $m_{\mu\mu}$ in the GJ frame; curves are for generated Monte Carlo events.

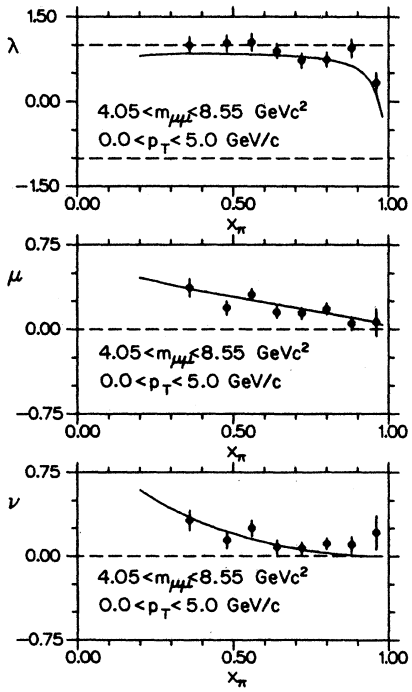

FIG. 34. Result for λ, μ, and ν as a function of x_π in the GJ frame; curves are for generated Monte Carlo events.

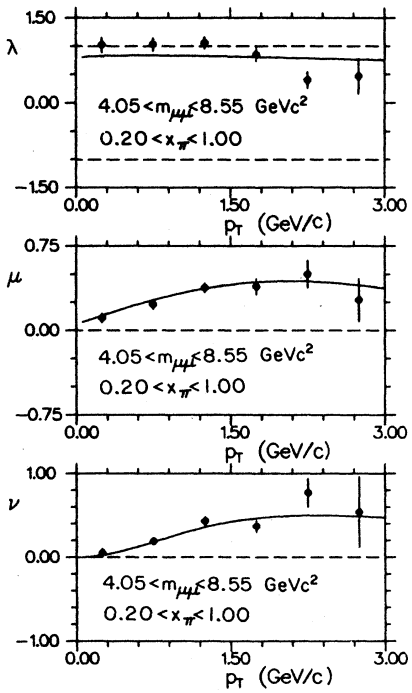

FIG. 36. Result for λ, μ, and ν as a function of P_T in the GJ frame; curves are for generated Monte Carlo events.

TABLE VIII. Angular-distribution fit results.

Frame	x_π range Low	x_π range High	$m_{\mu\mu}$ range Low (GeV/c^2)	$m_{\mu\mu}$ range High (GeV/c^2)	p_T range Low (GeV/c)	p_T range High (GeV/c)	λ	σ_λ	μ	σ_μ	ν	σ_ν	χ^2/N_{DF}	Prob.
GJ	0.28	0.44	4.05	8.55	0.00	5.00	0.99	0.15	0.37	0.08	0.32	0.09	20.44/16	0.201
GJ	0.44	0.52	4.05	8.55	0.00	5.00	1.03	0.14	0.19	0.06	0.14	0.07	78.24/73	0.316
GJ	0.52	0.60	4.05	8.55	0.00	5.00	1.05	0.15	0.31	0.05	0.25	0.07	79.08/78	0.445
GJ	0.60	0.68	4.05	8.55	0.00	5.00	0.89	0.13	0.15	0.05	0.08	0.06	112.30/78	0.007
GJ	0.68	0.76	4.05	8.55	0.00	5.00	0.72	0.13	0.14	0.05	0.07	0.05	94.30/78	0.101
GJ	0.76	0.84	4.05	8.55	0.00	5.00	0.74	0.13	0.18	0.05	0.11	0.05	105.98/79	0.023
GJ	0.84	0.92	4.05	8.55	0.00	5.00	0.94	0.16	0.05	0.06	0.10	0.07	103.35/81	0.048
GJ	0.92	1.00	4.05	8.55	0.00	5.00	0.33	0.18	0.06	0.12	0.21	0.15	27.56/18	0.069
GJ	0.20	1.00	4.05	4.50	0.00	5.00	0.86	0.10	0.32	0.03	0.32	0.04	71.43/73	0.530
GJ	0.20	1.00	4.50	4.95	0.00	5.00	1.04	0.12	0.32	0.05	0.30	0.04	88.97/74	0.113
GJ	0.20	1.00	4.95	5.40	0.00	5.00	1.12	0.15	0.34	0.06	0.37	0.07	67.32/74	0.695
GJ	0.20	1.00	5.40	6.30	0.00	5.00	1.00	0.13	0.27	0.05	0.28	0.07	89.55/75	0.120
GJ	0.20	1.00	6.30	7.20	0.00	5.00	0.99	0.21	0.23	0.07	0.28	0.09	115.79/76	0.002
GJ	0.20	1.00	7.20	8.55	0.00	5.00	1.06	0.29	0.10	0.13	0.00	0.13	15.46/18	0.630
GJ	0.20	1.00	4.05	8.55	0.00	0.50	1.02	0.13	0.11	0.04	0.05	0.05	96.40/73	0.035
GJ	0.20	1.00	4.05	8.55	0.50	1.00	1.03	0.11	0.23	0.04	0.19	0.04	101.18/73	0.016
GJ	0.20	1.00	4.05	8.55	1.00	1.50	1.06	0.10	0.38	0.04	0.43	0.05	95.55/68	0.015
GJ	0.20	1.00	4.05	8.55	1.50	2.00	0.85	0.12	0.39	0.07	0.37	0.07	71.63/68	0.358
GJ	0.20	1.00	4.05	8.55	2.00	2.50	0.40	0.14	0.50	0.12	0.77	0.17	16.07/17	0.519
GJ	0.20	1.00	4.05	8.55	2.50	3.00	0.47	0.31	0.27	0.19	0.54	0.42	15.61/16	0.481
CS	0.28	0.44	4.05	8.55	0.00	5.00	1.37	0.19	0.19	0.05	0.22	0.07	21.11/14	0.099
CS	0.44	0.52	4.05	8.55	0.00	5.00	1.19	0.18	0.02	0.06	0.11	0.07	84.01/70	0.121
CS	0.52	0.60	4.05	8.55	0.00	5.00	1.22	0.18	0.10	0.05	0.19	0.09	84.93/74	0.181
CS	0.60	0.68	4.05	8.55	0.00	5.00	0.97	0.13	−0.01	0.06	0.04	0.06	98.67/78	0.057
CS	0.68	0.76	4.05	8.55	0.00	5.00	0.86	0.14	0.02	0.05	0.05	0.05	101.65/79	0.044
CS	0.76	0.84	4.05	8.55	0.00	5.00	0.88	0.16	0.08	0.05	0.06	0.06	94.54/78	0.098
CS	0.84	0.92	4.05	8.55	0.00	5.00	1.12	0.18	−0.12	0.06	0.18	0.06	110.69/79	0.011
CS	0.92	1.00	4.05	8.55	0.00	5.00	0.12	0.29	0.04	0.08	0.14	0.22	19.07/17	0.324
CS	0.20	1.00	4.05	4.50	0.00	5.00	1.21	0.12	0.17	0.03	0.22	0.04	62.55/68	0.664
CS	0.20	1.00	4.50	4.95	0.00	5.00	1.16	0.15	0.09	0.04	0.21	0.04	67.53/68	0.493
CS	0.20	1.00	4.95	5.40	0.00	5.00	1.47	0.18	0.14	0.06	0.27	0.06	67.19/71	0.606
CS	0.20	1.00	5.40	6.30	0.00	5.00	1.25	0.16	0.10	0.05	0.25	0.06	60.47/71	0.809
CS	0.20	1.00	6.30	7.20	0.00	5.00	1.13	0.20	0.02	0.07	0.23	0.09	94.89/75	0.060
CS	0.20	1.00	7.20	8.55	0.00	5.00	0.85	0.41	0.08	0.20	0.03	0.13	11.08/20	0.944
CS	0.20	1.00	4.05	8.55	0.00	0.50	1.10	0.13	0.05	0.03	0.03	0.04	112.66/76	0.004
CS	0.20	1.00	4.05	8.55	0.50	1.00	1.19	0.12	0.09	0.04	0.14	0.03	98.96/71	0.016
CS	0.20	1.00	4.05	8.55	1.00	1.50	1.32	0.13	0.16	0.04	0.31	0.04	76.17/71	0.316
CS	0.20	1.00	4.05	8.55	1.50	2.00	1.04	0.17	0.08	0.05	0.23	0.06	71.07/70	0.442
CS	0.20	1.00	4.05	8.55	2.00	2.50	0.91	0.33	0.29	0.15	0.43	0.19	14.73/13	0.325
CS	0.20	1.00	4.05	8.55	2.50	3.00	1.29	0.39	0.37	0.24	0.73	0.29	20.72/17	0.239
UC	0.28	0.44	4.05	8.55	0.00	5.00	1.43	0.41	−0.11	0.09	0.22	0.13	7.34/10	0.693
UC	0.44	0.52	4.05	8.55	0.00	5.00	1.25	0.17	−0.23	0.04	0.18	0.05	95.46/74	0.047
UC	0.52	0.60	4.05	8.55	0.00	5.00	1.12	0.17	−0.17	0.04	0.22	0.07	74.36/73	0.434
UC	0.60	0.68	4.05	8.55	0.00	5.00	1.04	0.15	−0.14	0.05	0.08	0.05	86.51/74	0.152
UC	0.68	0.76	4.05	8.55	0.00	5.00	0.90	0.14	−0.10	0.05	0.08	0.05	95.34/74	0.048
UC	0.76	0.84	4.05	8.55	0.00	5.00	0.93	0.14	−0.05	0.05	0.02	0.05	100.48/72	0.015
UC	0.84	0.92	4.05	8.55	0.00	5.00	0.84	0.14	−0.22	0.05	0.19	0.07	118.18/73	0.001
UC	0.92	1.00	4.05	8.55	0.00	5.00	0.21	0.37	0.10	0.06	0.09	0.18	22.86/18	0.196
UC	0.20	1.00	4.05	4.50	0.00	5.00	1.18	0.14	−0.08	0.03	0.20	0.03	73.27/71	0.403
UC	0.20	1.00	4.50	4.95	0.00	5.00	1.34	0.13	−0.14	0.04	0.23	0.04	75.56/72	0.364
UC	0.20	1.00	4.95	5.40	0.00	5.00	1.39	0.16	−0.15	0.04	0.26	0.05	97.12/74	0.037
UC	0.20	1.00	5.40	6.30	0.00	5.00	1.20	0.14	−0.04	0.04	0.21	0.06	107.18/74	0.007
UC	0.20	1.00	6.30	7.20	0.00	5.00	1.09	0.19	−0.19	0.07	0.29	0.09	89.93/74	0.100
UC	0.20	1.00	7.20	8.55	0.00	5.00	0.76	0.30	−0.06	0.12	−0.03	0.17	11.57/19	0.903

TABLE VIII. (*Continued*).

Frame	x_π range Low	x_π range High	$m_{\mu\mu}$ range Low (GeV/c^2)	$m_{\mu\mu}$ range High (GeV/c^2)	p_T range Low (GeV/c)	p_T range High (GeV/c)	λ	σ_λ	μ	σ_μ	ν	σ_ν	χ^2/N_{DF}	Prob.
UC	0.20	1.00	4.05	8.55	0.00	0.50	1.05	0.13	−0.02	0.03	0.03	0.04	105.02/76	0.015
UC	0.20	1.00	4.05	8.55	0.50	1.00	1.11	0.11	−0.08	0.03	0.14	0.03	96.66/75	0.047
UC	0.20	1.00	4.05	8.55	1.00	1.50	1.35	0.13	−0.10	0.04	0.27	0.04	91.65/73	0.069
UC	0.20	1.00	4.05	8.55	1.50	2.00	1.09	0.17	−0.22	0.04	0.23	0.06	62.88/70	0.714
UC	0.20	1.00	4.05	8.55	2.00	2.50	1.19	0.41	−0.01	0.12	0.30	0.18	10.04/13	0.691
UC	0.20	1.00	4.05	8.55	2.50	3.00	1.91	0.76	−0.36	0.14	0.57	0.32	14.71/14	0.398

distributions for $|\cos\theta| < 0.6$ as a function of p_T. A clear $\cos 2\phi$ dependence is observed which increases with p_T. As will be discussed below the existence of this term is not expected, given the values of λ observed.

Figures 34–36 (and Table VIII) give the results for λ, μ, and ν in the t-channel (GJ) frame as functions of x_π, $m_{\mu\mu}$, and p_T. This frame is used because the detector acceptance is the broadest here and because it has been used to describe interesting model predicitions.[8] The solid curves in Figs. 34–36 are an empirical fit to the distributions and are used in the simulation of the detector response. They have no fundamental significance.

To test the consistency of the results the parameters λ, μ, ν were also determined in the CS and UC frames. Results in the GJ and UC frames were transformed to the CS frame, as described in Appendix E, and compared. The three determinations agreed to within a standard deviation.

On purely kinematic grounds the parameters μ and ν are expected to approach zero like $\rho = p_T/m_{\mu\mu}$ and ρ^2, respectively.[5] Figure 37 shows the measurements of λ, μ, ν as a function of ρ. This requirement is found to be satisfied.

2. *Test of the Callan-Gross relation*

As noted in Sec. I, the Callan-Gross relation predicts that $1-\lambda = 2\nu$, aside from small corrections associated with intrinsic transverse momenta of the constituents. These corrections are estimated to be less than 0.05. Figure 38 shows the quantity $2\nu-(1-\lambda)$ as a function of the

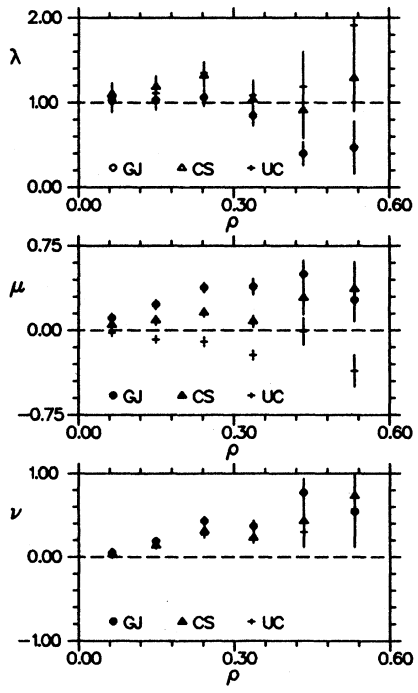

FIG. 37. Results for λ, μ, and ν as a function of $\rho \equiv p_T/m_{\mu\mu}$ in the Gottfried-Jackson, Collins-Soper, and u-channel reference frames.

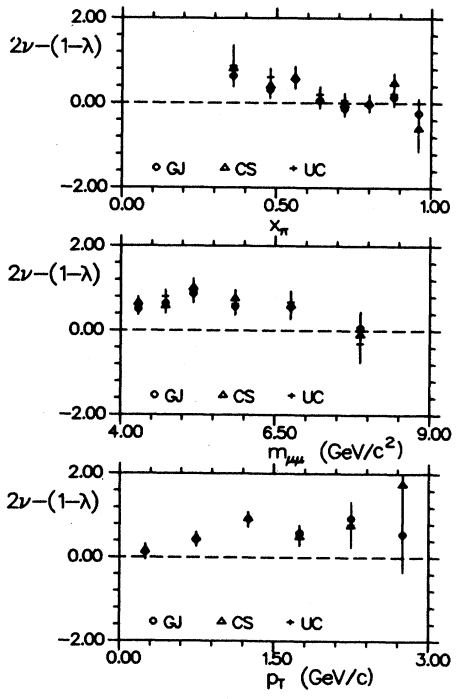

FIG. 38. Test of the relation $1-\lambda = 2\nu$ in the three kinematic variables, in the range $0.0 < p_T < 5.0$ GeV/c, $4.05 < m_{\mu\mu} < 8.55$ GeV/c^2, $0.2 < x_\pi < 1.0$. Results are shown for the Gottfried-Jackson, Collins-Soper, and u-channel reference frames.

three kinematic variables, in the three reference frames. The relation is violated in all three frames except at small p_T. The NA10 Collaboration has reported similar results as a function of p_T (Ref. 26). We know of no models in the literature which predict this effect.

3. *Higher twist*

In Sec. I the influence of higher-twist effects on the $\cos\theta$ distributions at large x_π was discussed. The model of Berger and Brodsky[8] was described, which predicts that, as $x_\pi \to 1$,

$$d\sigma \propto (1-x_\pi)^2(1+\cos^2\theta)+\frac{4x_\pi^2\langle k_T^2\rangle}{9m_{\mu\mu}^2}\sin^2\theta \ .$$

Thus, at high x_π, longitudinal photon polarization is predicted to dominate over transverse. The implications of this model for the structure functions were addressed in Sec. IV. The predicted $(1-x_\pi)^2$ behavior in the pion structure function was not seen but there are some evidence for the term proportional to $1/m_{\mu\mu}^2$, with $\langle k_T^2\rangle = 0.8\pm0.3$ (GeV/c)^2, although the $1/m_{\mu\mu}^2$ behavior *per se* was not verified. The model predicts a much more striking effect in the angular distributions: namely, that λ should change from near $\lambda=1$ at low x_π to $\lambda=-1$ as $x_\pi \to 1$.

Figure 32 shows λ in the t-channel (GJ) frame as a function of x_π for the mass range $4.05 < m_{\mu\mu} < 4.95$ GeV/c^2. The mass range used here is lower to enhance the $1/m_{\mu\mu}^2$ effect. The results show clearly that λ decreases at large x_π. Two curve are shown in Fig. 32. The dashed curve shows the expected variation of λ for the form of the cross section given above. The solid curve is based on a modified form of the cross section in which

$$d\sigma \propto (1-x_\pi)^\beta(1+\cos^2\theta)+\frac{4x_\pi^2\langle k_T^2\rangle}{9m_{\mu\mu}^2}\sin^2\theta \ ,$$

with $\beta=1.22$ as measured in this experiment rather than the value $\beta=2$ predicted by the model. The figure shows that this modification is needed to accommodate the data. Both curves use $\langle k_T^2\rangle = 0.8$ (GeV/c)^2, the value determined from the structure function analysis. The pure Berger-Brodsky curve can be made to fit these results for λ only by requiring $\langle k_T^2\rangle$ to be ~ 0.1 (GeV/c)^2; a value much lower than the authors suggest.[8]

As described in Sec. I, the model also predicts a ϕ dependence for the cross section. For $\beta=2$, the measured value of μ is not in agreement with the prediction.

We conclude that there is significant evidence in support of longitudinal polarization at large x_π. This may be due to the higher-twist effects proposed by Berger and Brodsky or some other source. These data do not permit a determination of the mass dependence of the effect in the region $m_{\mu\mu} > 4$ GeV/c^2. Work in progress on the lower-mass data of this experiment suggests a substantial enhancement of the effect. This emphasizes the importance of using the same mass interval for comparison of results on longitudinal polarization from different experiments.

VII. DISCUSSION AND CONCLUSIONS

We have presented the results of a study of continuum muon-pair production in an apparatus with particularly good acceptance at large x_F. For the data with $4.05 < m_{\mu\mu} < 8.55$ GeV/c^2 the mass spectrum, pion and nucleon structure functions, and the K factor are in good agreement with earlier determinations by NA3 and NA10. The cross section above the Υ resonances is larger than predicted by QCD evolution applied to our measurements at lower masses but the systematic errors are $\sim 25\%$.

A new effect, not reported before, is a cross-section component at low mass and large x_π which is not well described by the Drell-Yan formalism. An analysis of the helicity angular distributions indicates a large degree of longitudinal virtual-phonon polarization in this region.

This kinematic interval is the one expected for higher-twist processes and we have compared the data with a model of Berger and Brodsky for these effects. Their model predicts a $1/m_{\mu\mu}^2$ term in the pion structure function, associated with a $\sin^2\theta$ term in the angular distribution. The mass range of the data sample reported here is too narrow to allow a determination of the mass dependence of the effect but the pion structure function is consistent with a nonzero intercept at high x_π. The strength of the longitudinal polarization is consistent with the size of this intercept, as predicted. One feature of the data, in disagreement with the model, is the shape of the pion structure function at intermediate x_π which is $(1-x_\pi)^{1.27}$ rather than $(1-x_\pi)^2$.

It is interesting to note that the s dependence of the longitudinal photon polarization at fixed mass is rather different than that of the Drell-Yan continuum. A comparison with results from Ref. 2 indicates that at a beam energy of 80 GeV the effect is a larger fraction of the high x_F continuum than that at 250 GeV.

We have also reported measurements of the p_T spectra of the pairs. We observe a marked softening of the p_T spectrum at large x_F. No detailed comparison with predictions has been made in this analysis but the data are presented to facilitate such work. The results presented here show good agreement with other measurements where comparison is possible.

We have presented measurements of the three parameters λ,μ,ν which characterize the helicity angular distribution of the pairs. Results are given as a function of $m_{\mu\mu}$, p_T, and x_π. As noted above, evidence is seen of λ approaching -1 at large x_π. A $\cos2\phi$ term is observed in the angular distribution, in agreement with other experiments, but the size of the effect violates the analog of the Callan-Gross relation for this process.

ACKNOWLEDGMENTS

We are pleased to acknowledge many fruitful discussions of theoretical questions with Ed Berger and Wu-Ki Tung. Klaus Freudenreich has been especially helpful in discussing experimental issues and in facilitating comparison with the NA10 results. We gratefully acknowledge

the dedicated work of the technical support groups both at our home institutions and at Fermilab. The data for this experiment were obtained at Fermi National Accelerator Laboratory and the work was supported by the U.S. Department of Energy under Contracts Nos. DE-AC02-76ER03072 and W-7405-ENG-82-KA0101, and by the National Science Foundation, Grant No. 83-03203. This work was presented as a thesis to the Department of Physics, The University of Chicago, by J. S. Conway in partial fulfillment of the requirements for the Ph.D degree.

APPENDIX A: MONTE CARLO GENERATION SPECTRUM

Monte Carlo events were generated from the following (partially *ad hoc*) expression for the dimuon cross section:

$$\frac{d^5\sigma}{dx_\pi dx_N dp_T d\Omega}=\frac{4\pi\alpha^2}{9s}\left[\frac{F_\pi^v(x_\pi)G_N(x_N)+F_\pi^s(x_\pi)H_N(x_N)}{(x_\pi x_N)^2}\right]\frac{5(a/b)(p_T/b)^{a-1}}{[1+(p_T/b)^a]^6}$$
$$\times\frac{3}{16\pi}\left[1+\cos^2\theta+\frac{A_0}{2}(1-3\cos^2\theta)+A_1\sin 2\theta\cos\phi+\frac{A_2}{2}\sin^2\theta\cos 2\phi\right].$$

The functions F_π^v, F_π^s, G_N, and H_N were defined above in Sec. IV, with $Z/A=0.405$ for this experiment. Their component functions are parametrized as

$$F_\pi^v(x_\pi)=A_\pi^v\left[x_\pi^\alpha(1-x_\pi)^\beta+\gamma\frac{2x_\pi^2}{9m_{\mu\mu}^2}\right],$$
$$F_\pi^s(x_\pi)=A_\pi^s(1-x_\pi)^\delta,$$
$$x_N u_p^v(x_N)=A_p^u x_N^\mu(1-x_N)^\nu,$$
$$x_N d_p^v(x_N)=A_p^d x_N^\mu(1-x_N)^{\nu+1},$$
$$x_N u_p^s(x_N)=A_p^s(1-x_N)^\zeta.$$

The sum rules in the next section constrain the A_π and A_p coefficients. The values of the parameters used are $\alpha=0.60$, $\beta=1.26$, $\gamma=0.95$, $g_\pi=0.47$, $\delta=8.4$, $\mu=0.51$, $\nu=2.11$, $g_p=0.48$, and $\zeta=9.0$.

The p_T dependence is determined by the values of a and b, which are functions of x_F and $m_{\mu\mu}$:

$$a(x_F,m_{\mu\mu})=(a_0+a_1x_F)(1-a_2x_F)(1-a_3/m_{\mu\mu}^2)\times[1-(m_{\mu\mu}/a_4)^2]$$

and

$$b(x_F,m_{\mu\mu})=b_0(1+b_1x_F)(1-b_2|x_F|^{b_3})\times(1-b_4/m_{\mu\mu}^3).$$

The values of the parameters used are $a_0=2.35$, $a_1=0.58$, $a_2=0.334$, $a_3=2.88$, $a_4=30.9$, $b_0=2.74$, $b_1=-0.140$, $b_2=0.67$, $b_3=9.08$, and $b_4=2.92$.

The angular distributions are determined by the A_i:

$$A_0=\frac{4\xi}{m_{\mu\mu}^2}+\frac{\rho^2}{3(1+\rho^2)^2}+\frac{8\gamma x_\pi/9m_{\mu\mu}^2}{2x_\pi^\alpha(1-x_\pi)^\beta+4\gamma x_\pi/9m_{\mu\mu}^2},$$

$$A_1=\frac{3(1-x_\pi)\rho(1-\rho^2)}{(1+\rho^2)^2}+\frac{2(x_\pi\gamma/m_{\mu\mu}^2)^{1/2}(1-x_\pi)^{(1+\beta)/2}}{6x_\pi^\alpha(1-x_\pi)^\beta+4\gamma x_\pi/3m_{\mu\mu}^2},$$

$$A_2=\frac{32(1-x_\pi)^2\rho^2}{(1+5\rho^2)^2},$$

where $\rho\equiv p_T/m_{\mu\mu}$ and with the constants $\xi=0.3$ $(\mathrm{GeV}/c^2)^2$, $\alpha=0.37$, $\beta=1.22$, and $\gamma=0.8$ $(\mathrm{GeV}/c^2)^2$.

APPENDIX B: STRUCTURE-FUNCTION NORMALIZATION RULES

The momentum and valence number conservation sum rules may be written

$$\int_0^1\frac{F_\pi^v(x_\pi)}{x_\pi}dx_\pi=1,$$
$$2\int_0^1F_\pi^v(x_\pi)dx_\pi+6\int_0^1F_\pi^s(x_\pi)dx_\pi=1-g_\pi,$$
$$\int_0^1u_p^v(x_N)dx_N=2,\quad\int_0^1d_p^v(x_N)dx_N=1,$$
$$\int_0^1x_Nu_p^v(x_N)dx_N+\int_0^1x_Nd_p^v(x_N)dx_N+5\int_0^1x_Nu_p^s(x_N)dx_N=1-g_p,$$

where g_π and g_p are the pion and proton gluon momentum fractions. Given the parametrizations from the previous section, the sum rules place constraints on the parameters above:

$$A_\pi^v=[B(\alpha,\beta+1)]^{-1},$$
$$A_\pi^s=\frac{1+\delta}{6}\left[1-g_\pi-\frac{2B(\alpha+1,\beta+1)}{B(\alpha,\beta+1)}\right],$$
$$A_p^u=2[B(\mu,\nu+1)]^{-1},\quad A_p^d=[B(\mu,\nu+2)]^{-1},$$
$$A_p^s=\frac{1+\zeta}{5}\left[1-g_p-\frac{2B(\mu+1,\nu+1)}{B(\mu,\nu+1)}-\frac{B(\mu+1,\nu+2)}{B(\mu,\nu+2)}\right],$$

where $B(x,y)\equiv\Gamma(x)\Gamma(y)/\Gamma(x+y)$ is the Euler beta function.

APPENDIX C: STRUCTURE-FUNCTION PROJECTION

The method for projecting out points of the hadronic structure functions uses the fact that if the y_c^{ij} are the corrected number of events for bins centered at x_π^i and x_N^j, then summing over x_N (index j) at a fixed interval in x_π (index i) gives

$$\sum_j y_c^{ij}=KL\frac{4\pi\alpha^2}{9s}\int_{\Delta x_\pi^i}\frac{dx_\pi}{x_\pi^2}\int_{x_N^{\rm lo}}^{x_N^{\rm hi}}\frac{dx_N}{x_N^2}[F_\pi^v(x_\pi)G_N(x_N)+F_\pi^s(x_\pi)H_N(x_N)].$$

Here L is the integrated luminosity. Thus, if we wish to know $F_\pi^v(x_\pi^i)$ the integral over x_π can be approximated using the central value of the bin in x_π, so that we get

$$F_\pi^v(x_\pi^i)\simeq\frac{9s}{4\pi\alpha^2}\sum_j\frac{y_c^{ij}}{KL}\frac{x_\pi^{i2}}{\Delta x_\pi^i}I_G^{-1}-F_\pi^s(x_\pi^i)\frac{I_H}{I_G},$$

where

$$I_G\equiv\int_{x_N^{\rm lo}}^{x_N^{\rm hi}}\frac{dx_N}{x_N^2}G_N(x_N)\quad\text{and}\quad I_H\equiv\int_{x_N^{\rm lo}}^{x_N^{\rm hi}}\frac{dx_N}{x_N^2}H_N(x_N).$$

Similarly for $G_N(x_N)$,

$$G_N(x_N^j)\simeq\frac{9s}{4\pi\alpha^2}\sum_i\frac{y_c^{ij}}{KL}\frac{x_N^{j2}}{\Delta x_N^j}I_V^{-1}-H_N(x_n^j)\frac{I_S}{I_V}.$$

APPENDIX D: CDHS AND CCFRR STRUCTURE-FUNCTION PARAMETRIZATION

The parametrization of the CERN-Dortmund-Heidelberg-Saclay (CDHS) nucleon structure functions here is the one used by NA10 in their structure function analysis.[17] For the structure functions we write

$$x_N u_p^V(x_N)=A_u x_N^\alpha(1-x_N)^\beta(1+\gamma x_N^{\alpha'}),$$
$$x_N d_p^V(x_N)=A_d x_N^\alpha(1-x_N)^{\beta+1}(1+\gamma x_N^{\alpha'}),$$
$$x_N u_p^S(x_N)=A_s(1-x_N)^\delta.$$

The exponents evolve with $Q^2=m_{\mu\mu}^2$, for example, $\alpha=\alpha(\bar{s})$ where

$$\bar{s}\equiv\ln\left[\frac{\ln(m_{\mu\mu}^2/\Lambda^2)}{\ln(m_0^2/\Lambda^2)}\right].$$

We use the values

$$m_0^2=5.0\ (\text{GeV}/c^2)^2,\quad\Lambda=0.3\ \text{GeV},$$
$$\alpha=0.3543+0.4122\bar{s},\quad\alpha'=1.5760+2.0170\bar{s},$$
$$\beta=3.8330+2.8680\bar{s},\quad\gamma=11.57,$$
$$\delta=7.417-1.138\bar{s}+13.22\bar{s}^2-4.996\bar{s}^3-1.86\bar{s}^4,$$
$$A_s=(0.507\,58+0.230\,06\bar{s}+0.067\,345\bar{s}^2)/2.8.$$

By valence normalization we get

$$2/A_u=B(\alpha,\beta+1)+\gamma B(\alpha+\alpha',\beta+1),$$
$$1/A_d=B(\alpha,\beta+2)+\gamma B(\alpha+\alpha',\beta+2),$$

where $B(x,y)\equiv\Gamma(x)\Gamma(y)/\Gamma(x+y)$ is Euler's beta function.

For the CCFRR structure function we have the parametrization of Purohit[19] in which

$$x_N u_p^V(x_N)=a x_N^b(1-x_N)^c Z(x_N,Q^2),$$
$$x_N d_p^V(x_N)=a c_d' x_N^b(1-x_N)^{c+1}Z(x_N,Q^2),$$
$$x_N u_p^S(x_N)=2/5x_N F_1(x_N,Q^2)-1/5x_N F_3(x_N,Q^2),$$

where

$$Z(x_N,Q^2)=1+(g-h\sqrt{x})\log_{10}[Q^2/(10\ \text{GeV}^2)],$$
$$x_N F_1(x_N,Q^2)=1/2d(1+ex_N)(1-x_N)^f Z(x_N,Q^2),$$
$$x_N F_3(x_N,Q^2)=a[1+c_d'(1-x_N)]x_N^b(1-x_N)^c Z(x_N,Q^2)$$

and by valence counting we get

$$c_d'=\frac{1}{2}\frac{B(b,c+1)\{1+g\log_{10}[Q^2/(10\ \text{GeV}^2)]\}-B(b+\frac{1}{2},c+1)h\log_{10}[Q^2/(10\ \text{GeV}^2)]}{B(b,c+2)\{1+g\log_{10}[Q^2/(10\ \text{GeV}^2)]\}-B(b+\frac{1}{2},c+2)h\log_{10}[Q^2/(10\ \text{GeV}^2)]}.$$

The parameters have the values $a=2.3691$, $b=0.5348$, $c=2.5473$, $d=1.6489$, $e=0.7607$, $f=2.5761$, $g=0.3324$, and $h=0.9512$.

APPENDIX E: TRANSFORMATION BETWEEN ANGULAR FRAMES

From the value of the angular coefficients λ, μ, and ν in a given reference frame the values of the coefficients in another frame can be calculated. The three frames used in this analysis are all related by a rotation about the y axis. For example, to translate from the GJ to CS coefficients we have the relation

$$\begin{bmatrix}\lambda\\ \mu\\ \nu\end{bmatrix}_{\rm CS}=\frac{1}{\Delta}\begin{bmatrix}1-\rho^2/2 & 3\rho & 3\rho^2/4\\ -\rho & 1-\rho^2 & \rho/2\\ \rho^2 & -2\rho & 1+\rho^2/2\end{bmatrix}\begin{bmatrix}\lambda\\ \mu\\ \nu\end{bmatrix}_{\rm GJ},$$

$$\Delta\equiv1+\rho^2+\rho^2\lambda/2-\rho\mu-\rho^2\nu/4,$$

$$|\rho|=|\tan\beta|=p_T/m_{\mu\mu}.$$

The angle of rotation β is the angle between the GJ and CS frames. The same transformation holds from UC to CS; the reverse transformations are obtained simply by replacing ρ with $-\rho$ everywhere. It is important to remember, however, that the sign of the angle β, and hence that of ρ, is determined by the convention used for the definition of the x axis (or equivalently, given a right-handed system, the y axis). We have chosen the y axis to be given by a unit vector parallel to the cross product of the target direction and the beam axis (in the GJ frame) in the muon-pair center-of-mass frame. Clearly, however, the choice of the sign of the y direction only changes ϕ to $\phi+\pi$, resulting in μ changing to $-\mu$ without affecting the other coefficients.

---

*Present address: CERN, CH-1211 Geneva 23, Switzerland.
†Present address: University of California, Santa Cruz, California 94305.
‡Present address: SLAC, Stanford, California 94305.
§Present address: INFN, I-10125 Torino, Italy.
**Present address: FONAR Corporation, Melville, New York 11747.
††Present address: Los Alamos National Laboratory, Los Alamos, New Mexico 87545.

[1]S. D. Drell and T. M. Yan, Phys. Rev. Lett. **25**, 316 (1970).
[2]S. Palestini *et al.*, Phys. Rev. Lett. **55**, 2649 (1985); S. Palestini, thesis, Princeton University, 1984.
[3]J. S. Conway, thesis, University of Chicago, 1987. The only essential difference of the analysis reported here from that of this paper is the addition of a correction for secondary interactions in the target. These corrections primarily affect the structure functions at very low x and hence the K factor.
[4]J. Cleymans and M. Kuroda, Nucl. Phys. **B155**, 480 (1979); Phys. Lett. **105B**, 68 (1981).
[5]C. S. Lam and W. K. Tung, Phys. Rev. D **18**, 2447 (1978); **21**, 2712 (1980).
[6]G. Altarelli, R. K. Ellis, and G. Martinelli, Nucl. Phys. **B157**, 461 (1979); J. Kubar-Andre and F. E. Paige, Phys. Rev. D **19**, 221 (1979); J. Kubar *et al.*, Nucl. Phys. **B175**, 251 (1980); E. L. Berger, in *Proceedings of the Workshop on Drell-Yan Processes,* Batavia, Illinois, 1982 (Fermilab, Batavia, 1982), p. 1.
[7]K. Kajantie, J. Lindfors, and R. Raitio, Phys. Lett. **74B**, 384 (1978); J. C. Collins, Phys. Rev. Lett. **42**, 291 (1978); J. Cleymans and M. Kuroda, Phys. Lett. **80B**, 385 (1979); R. L. Thews, Phys. Rev. Lett. **43**, 987 (1979); Phys. Lett. **100B**, 339 (1981).
[8]E. L. Berger and S. J. Brodsky, Phys. Rev. Lett. **42**, 940 (1979); E. L. Berger, Z. Phys. C **4**, 289 (1980); S. J. Brodsky, E. L. Berger, and G. P. Lepage, in *Proceedings of the Workshop on Drell-Yan Processes* (Ref. 6), p. 187; the factor of x_π^2 in the $\sin^2\theta$ term is mentioned in the last reference and in E. L. Berger (private communication).
[9]C. Biino *et al.*, Nucl. Instrum. Methods **A243**, 323 (1986).
[10]H. W. Atherton *et al.*, CERN Report No. 80-07, 1980 (unpublished).
[11]A. Bodek and J. L. Ritchie, Phys. Rev. D **23**, 1070 (1981).
[12]A reivew of cross-section measurements and a fit to their energy dependence is given by L. Lyons, Prog. Part. Nucl. Phys. **7**, 169 (1981).
[13]J. G. H. de Groot *et al.*, Phys. Lett. **82B**, 456 (1979); Z. Phys. C **1**, 143 (1979).
[14]A. J. Buras and K. J. F. Gaemers, Nucl. Phys. **B132**, 249 (1978).
[15]F. Eisele, in *Proceedings of the 21st International Conference on High Energy Physics,* Paris, France, 1982, edited by P. Petiau and M. Porneuf [J. Phys. (Paris) Colloq. **43**, C3-337 (1982)].
[16]A compilation of results from different experiments is given in P. K. Malhotra, in *Proceedings of the Workshop on Drell-Yan Processes* (Ref. 6), p. 217.
[17]B. Betev *et al.*, Z. Phys. C **28**, 9 (1985); B. Betev *et al.*, *ibid.* **28**, 15 (1985); B. Mours, thesis, L'Universite Louis Pasteur de Strasbourg, 1984.
[18]J. Badier *et al.*, Z. Phys. C **18**, 281 (1983).
[19]M. V. Purohit, thesis, California Institute of Technology, 1983; D. B. MacFarlane *et al.*, Z. Phys. C **26**, 1 (1984).
[20]H. Abramovicz *et al.*, Z. Phys. C **17**, 283 (1983).
[21]D. B. McFarlane *et al.*, Z. Phys. C **26**, 1 (1984); F. Bergsma *et al.*, Phys. Lett. **141B**, 129 (1984).
[22]J. Badier *et al.*, in *Proceedings of the 1979 International Symposium on Lepton and Photon Interactions at High Energies,* Batavia, edited by T. B. W. Kirk and H. D. I. Abarbanel (Fermilab, Batavia, Illinois, 1980), p. 161.
[23]The value $\Lambda=0.15$ is consistent with the determination from the EMC Collaboration, J. J. Aubert *et al.*, Nucl. Phys. **B272**, 158 (1986).
[24]G. Altarelli, G. Parisi, and R. Petronzio, Phys. Lett. **76B**, 356 (1978).
[25]M. P. F. Bordalo, thesis, Laboratoire de Physique Nucléaire et Hautes Energies, Orsay, 1986; P. Bordalo *et al.*, in *Proceedings of the International Europhysics on High Energy Physics,* Bari, Italy, 1985, edited by L. Nitti and G. Preparata (Laterza, Bari, 1983).
[26]M. Guanziroli *et al.*, CERN Report No. EP/87-199, 1987 (unpublished).